ACS OMEGA

Open Access

http://pubs.acs.org/journal/acsodf

Article

Scheelite Catalysts for Thermal Mineralization of Toluene: A Mechanistic Overview

Mohsin Jafar,[§] Adarsh Kumar,[§] Vinita G. Gupta, Avesh K. Tyagi, and Kaustava Bhattacharyya*

Cite This: *ACS Omega* 2025, 10, 13080−13104

Read Online

ACCESS | Metrics & More | Article Recommendations | Supporting Information

ABSTRACT: Toluene, a highly stable aromatic hydrocarbon, is utilized as a benchmark molecule for thermal mineralization by the catalytic community. Mostly, the catalysts used for toluene mineralization either use platinum group metals (PGM) as catalysts or are regulated by a plasma incinerator. Though these catalysts/processes promise better efficiency and lower reaction temperature, they are neither cost-effective nor do they produce thermally stable byproducts. However, most of the metal-oxide catalysts used for toluene degradation are less efficient owing to incomplete mineralization and formation of stable intermediates, which results in higher mineralization temperature. The present work showcases tungsten- and molybdenum-based Scheelites [$BaXO_4$ (X = W, Mo, and $Mo_{0.5}W_{0.5}$)], which have been utilized for toluene mineralization at ∼200 °C. The intermediates formed during adsorption and thermal reaction are deciphered as a function of temperature using in situ FT-IR studies including their kinetic behavior. These surface intermediates formed over the Scheelite catalysts under an oxidative/inert atmosphere elucidate the toluene mineralization mechanism as a function of temperature/time. The surface active sites for these oxide catalysts for both adsorption and formation of reaction intermediates are deciphered using detailed X-ray photoelectron spectroscopy (XPS) studies. It shows the effective role of the oxidation states of constituent oxides M−O (M = Mo/ W) in the reaction mechanism. Mineralization of *toluene* in a nonoxidative atmosphere shows a Mars and Van Krevelen (MVK) type of mechanism, suggesting participation of lattice oxygen for the catalytic reaction. To the best of our knowledge, this work represents one of the lowest temperatures achieved for toluene mineralization using oxide catalysts. The identification of reaction intermediates can guide further optimization efforts to minimize the mineralization temperature.

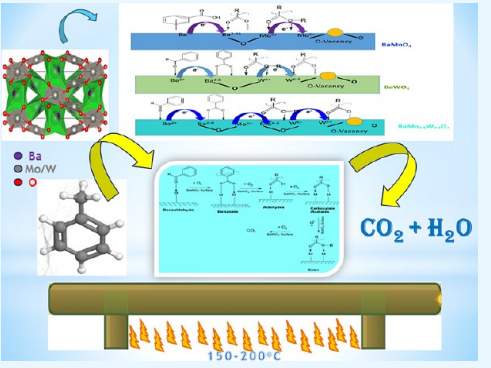

1. INTRODUCTION

In the recent past, there has been significant concern emerging for the detailed kinetic mechanisms to designate the mineralization of aromatic fuels using both thermal and photodriven catalysts and even by catalysts which are used for photothermal processes.[1] Though there have been quite a few proposals for understanding the photocatalytic mechanisms where photocatalytic oxidation is a promising flue gas purification technology, especially for degradation of volatile organic compound (VOC) like toluene,[2−4] yet thermal decomposition of toluene is not well understood due to complications in its measurement. Environmentally and biologically speaking, toluene is an irritant to the skin and mucous membrane and can act as an anesthetic to the central nervous system.[5,6] Long-term exposure to toluene can lead to neurasthenia and leukemia.[7,8] Conventional air purification methods, such as heat or catalytic combustion, biological filtration, membrane separation, and selective reduction technology, are limited in their ability to remove toluene.[9,10] Noble metal catalysts presently play a significant role in the catalytic degradation of toluene and possess greater catalytic degradation capability at lower temperatures.[11,12] Again, strong metal support interaction for the supported metal catalysts significantly alters the catalytic activity and the stability of the concerned catalysts.[13,14] In the study of catalytic oxidation of toluene, oxygen vacancy concentration is considered to be an important factor affecting the activity.[15−17] A comprehensive study of the adsorption and catalytic mechanism of toluene oxidation using TiO_2 as a photocatalyst is available in the literature.[18] In the photocatalytic process, surface −OH groups present over the photocatalyst surface interact with toluene, effectively regulating the adsorption and reaction phenomena.[19] The adsorption of the toluene over the catalytic surface was also speculated by a weak bonding using the π-aromatic ring of toluene with surface −OH groups of the catalytic surface of TiO_2.[20] The major products of photocatalytic degradation of toluene on TiO_2 were CO_2 and benzaldehyde, as illustrated by Ibusuki and Takeuchi,[21] and water vapor

Received: November 19, 2024
Revised: January 1, 2025
Accepted: January 10, 2025
Published: March 25, 2025

creates a positive effect in the photo-oxidation process. There are two types of hydroxyl groups present over TiO_2[22] and the interaction of isolated type and H-bonded hydroxyls on the surface of TiO_2 leading to different types of intermediates. The interaction of toluene with the hydroxyl groups of isolated types mainly leads to the formation of a stable intermediate, benzaldehyde, while the interaction with H-bonded hydroxyls leads to nearly complete degradation. However, relatively few studies have focused on the mechanisms of toluene mineralization with catalysts between adsorption and the different intermediates as a function of the temperature for the mineralization of toluene.

Recently, there has been quite a good understanding of the perovskites-like (ABO_3) doped $BaTiO_3$-based catalysts for coupling nonthermal plasma technology coupled with the catalytic degradation for toluene.[23] Similarly, the other perovskite-type oxides are also used as catalysts for efficient mineralization of toluene.[24,25] One of the typical examples is $LaMnO_3$, which is used as a catalyst for catalytic combustion of toluene; the change in the redox properties (of Mn^{6+}), which is tunable with the structural variation in such perovskite, makes it an active thermal catalyst around (180−220) °C under different external conditions.[26]

Recently, the Alvencar group reported a microwave-assisted hydrothermal-assisted Scheelites like $CaWO_4$ for mineralization of toluene at around ∼160−220 °C.[27] The Scheelites of the $BaXO_4$ (X = Mo and W) have interesting properties and, being a d^0 system, have definite oxidative catalytic properties. It becomes quite imperative to check their catalytic properties, for which, with toluene being a benchmark VOC, the mineralization would be improved as compared to that of the $CaWO_4$ system. To the best of our knowledge, this will be the first article to show the thermal catalytic properties for mineralization of toluene using a Scheelite at a temperature as low as 200 °C.

Toluene is a type II carcinogenic agent, an aromatic hydrocarbon, which is commonly used as an industrial feedstock and solvent. However, repeated exposure of toluene to pregnant ladies may increase the risk of damage to the fetus. More rigorous requirements for removing toluene from atmospheric air in recent eras necessitate the expansion of innovative cost-effective treatment alternatives. There are numerous physical and chemical gas cleaning methods such as biofiltration[28] bioremediation, biodegradation, absorption, incineration,[29] wet scrubbing, adsorption, and thermal and catalytic oxidation.[30] However, on the industrial scale, the toluene removal, as shown by Zhang et al.,[31] is usually done by plasma incineration[32] or by bioremediation[33] or by ozonolysis with Pt/MnO_2-type catalysts[34] using platinum group metals (PGM) as catalysts. These require either a plasma setup or PGM catalysts. However, the present catalyst, a Scheelite, usually a very robust, symmetric structure and scalable in nature mineralization of toluene at ∼200 °C, gives an option for industrial usage.

The complete mechanism for adsorption and mineralization of toluene in the presence and absence of air has been established for the three different catalysts $BaMoO_4$, $BaWO_4$, and Mo doped in the $BaWO_4$ catalytic surface. The catalytic reaction has been conducted under static conditions with extensive in situ FT-IR studies, which have been performed to establish the reaction intermediates as well as the reaction kinetics. The XPS studies have been performed over the catalyst and the used catalyst to decipher the active sites that are responsible for the process of adsorption and reaction. This article will lead to a new way for the researchers of the catalytic fraternity to envisage different Scheelites as thermal catalysts, as it explains the effect of thermal mineralization of toluene and the different intermediates formed over the surface. The effect of the surface O-vacancies is also elaborated in the present article.

2. EXPERIMENTAL SECTION

2.1. Synthesis of Catalysts. $BaMoO_4$, $BaWO_4$, and $BaMo_{0.5}W_{0.5}O_4$ were prepared by a coprecipitation method. A stoichiometric amount (1×10^{-2} mol) of barium nitrate [$Ba(NO_3)_2$] (99% purity, Sigma-Aldrich) was dissolved in 50 mL of distilled water in a glass beaker. In another glass beaker, 1×10^{-2} mol of sodium molybdate dihydrate [$Na_2MoO_4 \cdot 2H_2O$] (99% purity, Sigma-Aldrich) was dissolved in 50 mL of distilled water. Sodium molybdate solution was then added dropwise to the barium nitrate solution with constant stirring for better homogenization. Upon gradual addition of sodium molybdate solution, fine precipitate started to appear within the glass beaker. The precipitation was completed by adjusting the pH of the solution to 11 by addition of the required amount of NH_4OH solution. The mixture was allowed to be kept under constant stirring for 1 h. The solution was then centrifuged at 8000 rpm for 5 min for separation of the suspended precipitate. The separated solid was repeatedly washed and centrifuged with water and isopropyl alcohol to remove any soluble and unwanted impurities. A similar procedure was followed for $BaWO_4$ and $BaMo_{0.50}W_{0.50}O_4$ by using sodium tungstate dihydrate [$Na_2WO_4 \cdot 2H_2O$] (99% purity, Sigma-Aldrich) and a 1:1 mixture of sodium molybdate dihydrate and sodium tungstate dihydrate, respectively. The three obtained powders were then dried in an oven at 180 °C overnight.

2.2. Characterization. All the prepared nominal compositions were characterized thoroughly by powder X-ray diffraction (XRD) using a PANalytical X-pert pro powder diffractometer using Cu Kα radiation (λ = 1.5406 Å) in the two-theta range of (10−70)°. Raman samples were measured with a 632.8 nm line of a diode laser used for excitation, and the scattered light was analyzed using a 0.9 nm single stage monochromator coupled with a CCD detector. Laser Raman spectra were taken on a HORIBA JOBIN YVON, LabRam HR 800 spectrometer (180°); back-scattering geometry was used, excitation source was Ar^+ ion laser, spectral resolution was 2 cm^{-1}, and He−Ne laser (632.8 nm) was an excitation source. Transmission electron microscopy (TEM) data were obtained using a 200 kV FEI Tecnai T20 machine equipped with a LaB_6 filament. TEM samples were prepared by placing a drop of the ultrasonically dispersed powder (in alcohol) on a carbon-coated copper grid and drying in air. An X-ray photoelectron spectroscopy (XPS) study was performed using a Thermo Fisher Scientific NEXSA instrument operating at 12 kV anode voltage with 6.50 mA filament current (1486.6 eV Al K_α dual anode source). The data were taken at a pass energy of 50 eV at 9×10^{-8} mbar vacuum. As an internal reference for the absolute binding energy, the C-1s peak (284.5 eV) was used. All the deconvolutions are made by the CASA software with Voigt type peak having GL (75) to GL (30) without imparting any asymmetry. The baseline was made using the Shirley function. Error for the fitting of the Voigt curve is calculated from the (Adjoint R^2) value of 0.998 from origin software, which is obtained by using a nonlinear curve fitting using a

https://doi.org/10.1021/acsomega.4c10501
ACS Omega 2025, 10, 13080−13104

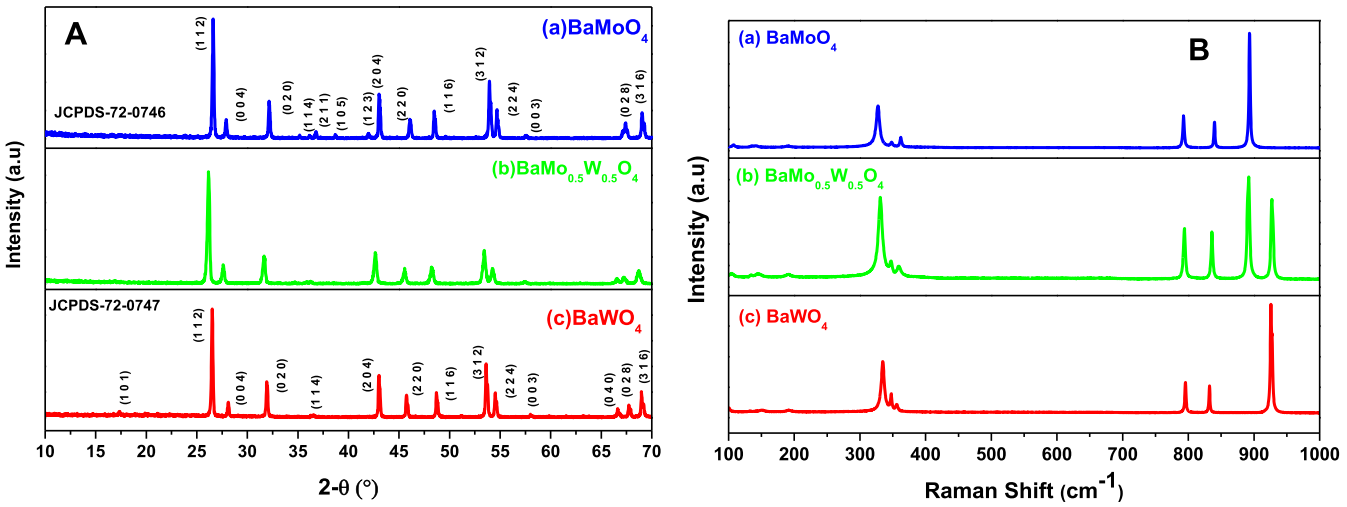

Figure 1. (A) XRD for the different catalysts: (a) $BaMoO_4$; (b) $BaMo_{0.5}W_{0.5}O_4$; and (c) $BaWO_4$; (B) Raman spectra for the different catalysts: (a) $BaWO_4$; (b) $BaMo_{0.5}W_{0.5}O_4$; and (c) $BaMoO_4$.

Voigt Curve (usually taken for the XPS data set) and taking the different values for fitting from the CASA software to calculate the regression of the error percentage.

2.3. In Situ FT-IR Studies. The present instrument of Bruker V70 with KBr beam splitters was utilized for taking the in situ FT-IR study data sets. The external unit XAS in the Bruker V70 for the in situ FT-IR studies possesses a SPECAC cell with a MCT detector (4000 −800) cm^{-1}. The cell used for in situ FT-IR has a volume of 80 cc attached on the right side of the main unit and is coupled with a high vacuum facility [turbo-molecular pump (air-cooled) and a dry roughing pump] achievable vacuum level 10^{-6} mbar. An in-built resistive heater can provide temperature variation from 25 to 800 °C along with the required safety features. It was typically used in transmission mode with suitable windows (ZnSe) and with provision of at least three inlet and outlet ports for evacuation and introduction of gases.

The in situ FT-IR experiments were conducted as follows. Initially, the catalysts are ground in a mechanical grinder at least for a day and then a self-supported pellet of 10 mm diameter 0.8 mm thick and 50−70 mg weight was made, which was then subjected to 10^{-4} mbar pressure and ∼(100−300) °C as a function of temperature (with increment of 100 °C) for around 3−6 h in order to clean the surface of the pellet, as shown in Figure 1. A pellet spectrum is recorded at 50 °C to understand the temperature effect over the pellet. The Figure S1 shows treatment for the $BaMO_4$ catalyst as a function of temperature and time. Further, the pellet is brought down to room temperature under vacuum, and the final spectra of the pellet are taken with a background spectrum of air. Post that, a background with the pellet is taken. This pellet was subsequently exposed to 40 cc of 474 ppm toluene−air or 40 cc of toluene−He mixture, prepared in a gas bulb externally, respectively. Normally, 32 scans with resolution 4 were coadded, and the spectra were recorded by using a similarly treated but unexposed pellet as background. The toluene sorption over the different self-supported catalyst pellets is initially monitored to understand the effect of adsorption. Subsequently to the adsorbed toluene over the catalytic surface, temperature is applied and different intermediates that are formed are studied as a function of temperature and time for the different catalysts.

3. RESULTS AND DISCUSSION

3.1. X-ray Diffraction (XRD). The powder XRD patterns of all the nominal compositions after overnight drying in an oven are exhibited in Figure 1A.

No diffraction peaks corresponding to reagents or any other impurity were observed in the diffraction patterns. Thus, it can be concluded that the compositions obtained by the coprecipitation route of synthesis are of pure phase. The obtained XRD patterns of the end member compositions are found to be in agreement with that reported in literature [PC-PDF card no. 72−0747 and 72−0746 respectively]. It is clearly evident from the powder X-ray diffraction pattern that both the end member as well as the non-end member nominal compositions have crystallized in a tetragonal unit cell with $I4_1/a$ space group symmetry. No gradual and visible peak shift was observed in the diffraction patterns due to the closely lying ionic radii of Mo^{6+} and W^{6+}.

3.2. Raman Spectroscopy. The system $BaW_xMo_{1-x}O_4$ ($0.0 \leq x \leq 1.0$) crystallizes in a Scheelite structure (space group: $I4_1/a$) and minimal (C_{4h}) point group with two formula units per unit cell. The group theoretical analysis predicts 26 optical vibration modes belonging to the following irreducible representations presented in eq 1

$$\Gamma_{tot} = 3A_g + 5B_g + 5E_g + 5A_u + 3B_u + 5E_u \quad (1)$$

The g-vibrational modes (Ag, Bg, and Eg) are only Raman active bands, which show change in the polarizability induced by the vibrational excitation.[35] The vibrational modes (A_u, B_u, and E_u) are both Raman and infrared active that occur due to the changes in the dipole moment during the vibration. The Raman bands over 300 cm^{-1} refer to the internal modes of MO_4 tetrahedra, and the Raman vibrations below 300 cm^{-1} wavenumbers are external phononic modes associated with the motion of the Ba^{2+} cations and rigid molecular units MO_4. Weak coupling is observed between the MO_4 tetrahedra and Ba^{2+} cations in the Scheelite structure, and the vibrational modes can be approximated to internal or external modes, wherein internal modes refer to vibrations happening in MO_4 tetrahedra. In the extrinsic modes, all three types of atoms, i.e., Ba, Mo/W, and O participate, wherein the modes at ∼100 and ∼130 cm^{-1} are the translational vibrational modes and those at ∼150 and ∼190 cm^{-1} are the rotational vibrational modes.

https://doi.org/10.1021/acsomega.4c10501
ACS Omega 2025, 10, 13080−13104

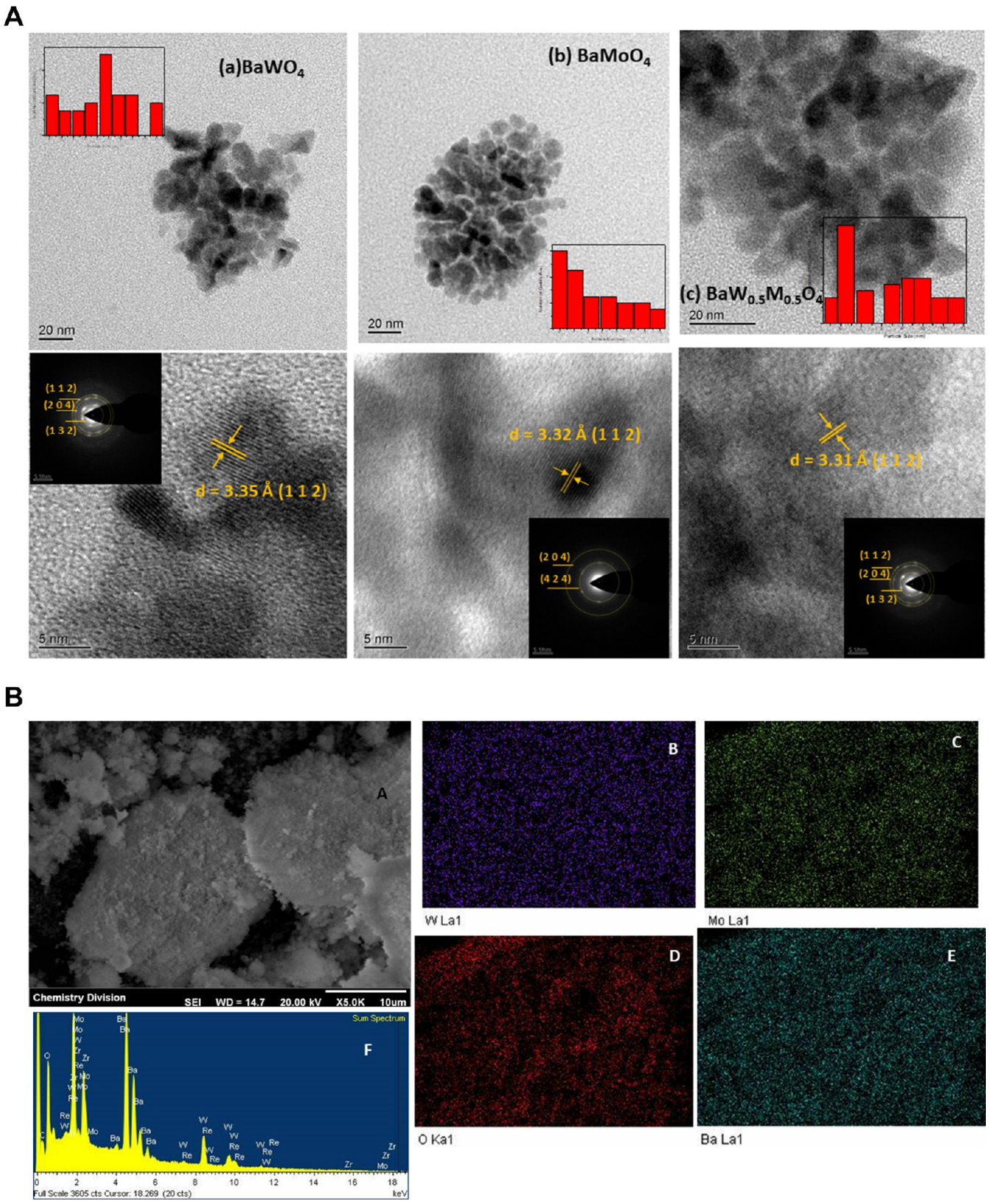

Figure 2. (A) Morphological features, crystallographic data, and particle size calculation from TEM and HRTEM data of (a) $BaWO_4$; (b) $BaMoO_4$; and (c) $BaW_{0.5}Mo_{0.5}O_4$; the inset in the top panel for each of the samples shows the particle size distribution, and the inset in the lower panel shows an indexed SAED pattern for all the samples. (B) Morphological feature shown with (A) SEM; elemental mapping of (B) W; (C) Mo; (D) O; and (E) Ba; and (F) EDS results for Ba, Mo, W, and O from the SEM data set.

Figure 1B shows the Raman spectra of all the nominal compositions in the system $BaWO_4$, $BaMoO_4$, and $Ba-Mo_{0.5}W_{0.5}O_4$. All the Raman modes can be identified as reported in the literature and described above as belonging to

https://doi.org/10.1021/acsomega.4c10501
ACS Omega 2025, 10, 13080−13104

the Scheelite-type crystal structure. The Raman modes at (795, 832, and 926) cm^{-1} are related to the stretching vibrations of the W−O bonds in $BaWO_4$ [Figure 1B(a)] and corresponding Raman modes at (792, 839, and 893) cm^{-1} are related to the stretching vibrations of the Mo−O bonds in $BaMoO_4$ [Figure 1B(c)] The Raman spectra of the end members $BaMoO_4$ and $BaWO_4$ are similar except that the highest frequency Raman mode appears at 924 cm^{-1} for $BaWO_4$ and 893 cm^{-1} for $BaMoO_4$. The intermediate nominal composition shows both Raman modes, indicating the presence of both MoO_4 and WO_4, as shown in $BaMo_{0.5}W_{0.5}O_4$ [Figure 1B(b)]; strong intense peaks at (925 and 893) cm^{-1} are assigned to A_g mode for $[MoO_4]^{2-}$ and $[WO_4]^{2-}$ units, respectively. The three Raman bands at (834, 358, and 329) cm^{-1} are attributed to B_g modes, while the peaks at (794 and 358) cm^{-1} are attributed to Eg internal mode. The Ag modes are observed at (329 and 196) cm^{-1}, and the band at 329 cm^{-1} is the superposition of ν_2Ag and ν_2Bg modes of vibrations.[36] It is interesting to note that in general, the Raman modes exhibit a blue shift on substituting Mo in $BaWO_4$ in the present series, which is because the higher the bond strength, the lower is the reduced mass in Mo−O and W−O bonds. Owing to lanthanide contraction, ionic radii of W^{6+} and Mo^{6+} are almost similar.[37] However, the bond length of W−O in $BaWO_4$ (1.8230 Å)[38] is longer than the bond length of Mo−O in $BaMoO_4$ (1.78 Å).[39] Also, the atomic mass of W is higher than that of Mo. Both these factors result in blue shift of Raman modes on $BaWO_4$ on successive substitution of W by Mo.

3.3. High Resolution Transmission Electron Microscopy. The morphological structure from the TEM study shows for the nano-Scheelites a spheroidal structure (Figure 2), with a distribution of particle size for all the $BaWO_4$, $BaMoO_4$, and $BaMo_{0.5}W_{0.5}O_4$ of around 6.2 nm [Figure 2a−c]. The *d*-spacing for the HRTEM data set for the Scheelite material is shown in the lower panel (Figure 2) and is indexed with the requisite plane concerning the materials.

The crystallographic understanding from the SAED patterns shows nanocrystalline materials that are indexed appropriately.

The SEM image for $BaMo_{0.5}W_{0.5}O_4$ shows the flat flowery structures. The elemental EDS mapping for Ba, W, Mo, and O shows equivalent presence of Mo and W in the same place along with Ba and O. The other SEM structures of $BaWO_4$ and that of $BaMoO_4$ are presented as Figures S6 and S7. The elemental analysis from the EDS spectra for all these samples is tabulated as Table S2, where it confirms the presence of Mo and W for $BaW_{0.5}Mo_{0.5}O_4$.

3.3.1. Catalytic Activity (Thermal Degradation of Toluene). The catalytic activity of the different catalysts was measured in static conditions in the in situ FT-IR cell, where the product obtained was only CO_2. The rate of the reaction or percent conversion of the toluene is calculated using the following equation. Figure 3 shows the percent conversion of toluene with the different catalysts, and it is obvious from Figure 4 that at 200 °C, the catalytic activity is in the order $BaMoO_4$ < $BaWO_4$ ≪ $BaMo_{0.5}W_{0.5}O_4$. The catalysts were utilized at different temperatures and have been recycled for at least three cycles. The different rates for these catalytic activities are studied based on the different intermediates that are formed over the surface of the catalysts and the effective change of the surface oxidation states, leading to the formation of different intermediates.

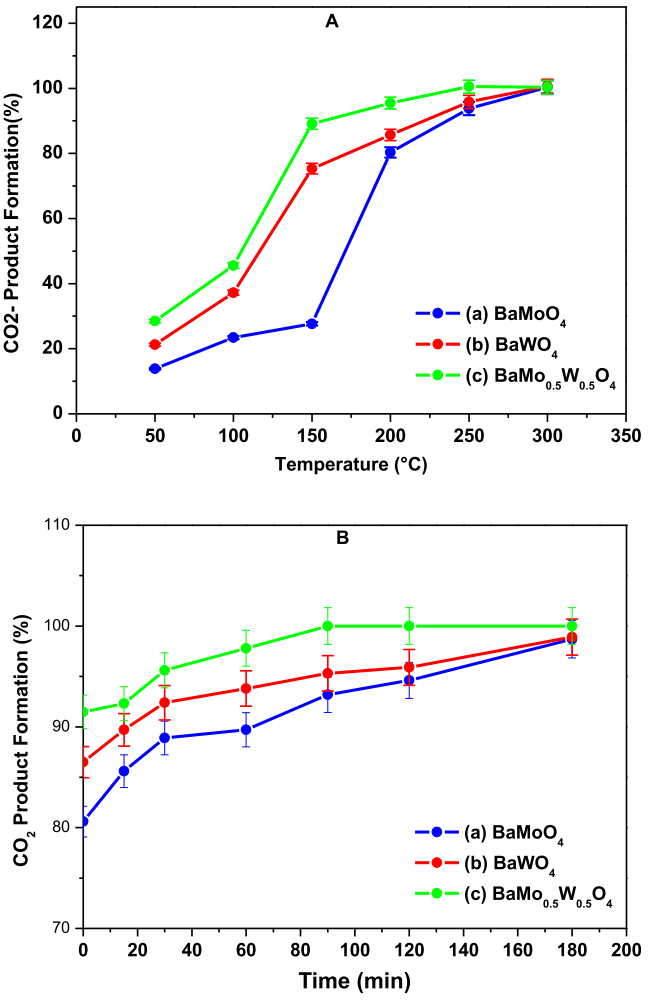

Figure 3. (A) Percentage toluene conversion (% CO_2 formation) formation as a function of temperature for the three catalysts and the support (a) $BaMoO_4$; (b) $BaWO_4$; and (c) $BaMo_{0.5}W_{0.5}O_4$; (B) plot of conversion (%) for the production of product CO_2 upon thermal mineralization of toluene in the presence of air at 200 °C for three different catalysts—(a) $BaMoO_4$; (b) $BaWO_4$; and (c) $BaMo_{0.5}W_{0.5}O_4$ (with error percentage).

$$\text{Conversion}(\%) = \frac{V_{CO_2}(\text{ml})}{A_{CO_2}(\text{ml})} \times 100 \quad (2)$$

Where V_{CO_2} = Volume of CO_2 produced as calculated from the FT-IR using calibration curve, A_{CO_2} = Stoichiometric amount of CO_2 to be produced by complete oxidation of toluene using the eq 3

$$C_7H_8 + 9O_2 \xrightarrow[\text{Temperature}]{\text{Catalyst}} 7CO_2 + 4H_2O \quad (3)$$

Volume of CO_2 to be produced Stoichiometrically = 7 × Volume of toluene in the static reactor, Volume of toluene present = Volume of toluene taken × 474 ppm × 3 = 40 × 474 × 10^{-6} cc × 3 = 5.7 × 10^{-2} cc.

Therefore, the total amount of CO_2 produced by complete oxidation of toluene = 0.06 × 6 = 0.36 cc = A_{CO_2}.

The conversion (%) as a function of temperature is an indicator of the behavior of the thermal catalyst at that particular temperature. Therefore, it is quite obvious that the $BaMoO_4$ catalyst almost degrades toluene at ∼250 °C to 90%.

https://doi.org/10.1021/acsomega.4c10501
ACS Omega 2025, 10, 13080−13104

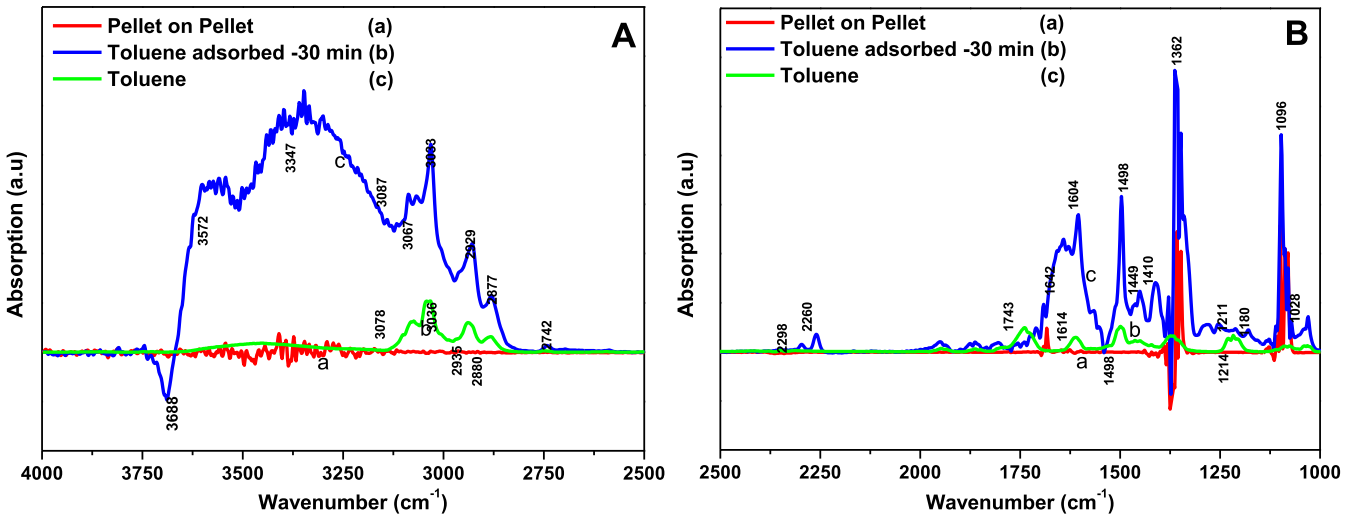

Figure 4. Adsorption of toluene and air over the $BaMoO_4$ catalyst; (a) vibrational spectra for the pellet spectra taken over $BaMoO_4$ pellet as baseline; (b) toluene spectra in air; and (c) toluene and air adsorbed over $BaMoO_4$ surface. (A) (4000−2500) cm^{-1} and (B) (2500−1000) cm^{-1}.

Table 1. Comparison of Different Catalysts for Thermal Mineralization of Toluene

S. no	type of catalyst	temperature for complete conversion (°C)	preparation method	reaction conditions	reference
1	K-OMS-2 (potassium−manganese oxide)	270	hydrothermal synthesis	continuous flow reactor with an internal diameter of 5 mm and toluene evaporating at 3 °C	41
2	CeO_2/g-Al_2O_3	250	impregnation method	N_2−gas mixture of 0.87 g/m^3 toluene and 20 vol % O_2 gas flow rate of 8.3×10^{-6} m^3/s	42
3	γ-Mn_2O_3	300	precipitation method		31
4	CeO_2-MOx (M = Mn, Zr and Ni)	261	co-preparation method	quartz tubular microreactor with a 6 mm diameter, dry air (20% O_2 diluted into pure N_2) contains 100 ppm toluene in mass flow controllers and purged in a microreactor	43
5	Mn-MIL-100 (MOF)	209	solvothermal method	1000 ppm toluene + 20 vol % O_2 balanced with Ar in a fixed-bed reactor	44
6	La-based ABO_3 (Perovskite catalysts)	220−445	solvothermal method	210 ppm toluene in nitrogen at a constant ratio of toluene/nitrogen and oxidant (air)	45
7	present work (Scheelite)	150−200	Co-precipitation	40 cc of 474 ppm toluene−air/He mixture 50−70 mg catalyst set	this paper

Similarly, if we compare the $BaWO_4$ catalyst, it is more reactive, as compared to that of $BaMoO_4$ and gives almost 98% degradation of toluene of value at ∼200 °C; however, the $BaMo_{0.5}W_{0.5}O_4$ catalyst shows almost 99.3 (almost 100% conversion) at 200 °C (Figure 3A). Figure 3A quite clearly shows that $BaMo_{0.5}W_{0.5}O_4$ is the best catalyst, and it completely mineralizes toluene at 200 °C, and post that, the activity almost saturates. Figure 3B shows a comparative presentation of the kinetics for all the catalysts as well as the support at 200 °C. It is quite evident here also that at around 100 min, the $BaMo_{0.5}W_{0.5}O_4$ catalyst mineralizes toluene (which can be taken as a representative benchmark molecule for VOCs) completely. However, at lower temperatures, on comparison, it is evident that the catalytic activity is in the order: $BaMo_{0.5}W_{0.5}O_4 \gg BaWO_4 > BaMoO_4$. The previous literature shows the complete mineralization of toluene by Mn-based catalysts at almost ∼250 to 300 °C.[32] CeO_2-based catalysts mainly containing Pt/Ni show complete degradation of toluene at lower temperatures ∼160−200 °C. The catalytic oxidation of toluene occurs by electron transfer between the metal oxide and the reactants, and the process is significantly influenced by the oxygen mobility and oxidizing capacity of the catalyst.[17] It is generally believed that the catalytic oxidation of toluene follows more the Mars-van Krevelen mechanism. The Dyson group has shown that the perovskite (ABO_3) is particularly versatile because their flexible composition, abundant defects, highly exposed active surfaces, and tunable redox properties can be used for thermal degradation of toluene, benzene, and xylene, where the different morphologies and structures of ABO_3 -PCs affect the packing density, porosity, specific surface area, and surface energy of the catalyst influence catalytic activity.[40] It can be clearly seen that by using the oxide type of materials, these Scheelite catalysts mineralize toluene at the lowest temperature (Table 1). That makes it quite imperative to understand how these catalysts behave in the degradation process and how the process of degradation occurs over the surface of these catalysts. To understand the different intermediates formed over the surface and the mechanism of the toluene degradation in oxidative and nonoxidative atmosphere, in situ FT-IR studies were carried out as portrayed below.

In order to understand the different intermediates formed during the thermal degradation of the toluene for the different catalysts of the present Scheelites, in situ FT-IR experiments were conducted to understand the overall mechanism for the

https://doi.org/10.1021/acsomega.4c10501
ACS Omega 2025, 10, 13080−13104

toluene mineralization. The mechanism will lead to the understanding for the activity of the different catalysts.

3.4. In Situ FT-IR Results. *3.4.1. $BaMoO_4$ Catalyst. 3.4.1.1. Adsorption of Toluene over $BaMoO_4$.* Figure 4A shows that there are 12 characteristic peaks of gas phase toluene, which are (3074, 3041, 2935, 2881, 2750, 1948, 1863, 1799, 1737, 1610, 1498, and 1461) cm^{-1}. Among them, 3074 and 3041 cm^{-1} are the C−H stretching vibration peaks on the aromatic ring. 2935 cm^{-1} is the antisymmetric stretching vibration peak of methyl. 2881 cm^{-1} is the symmetrical stretching vibration peak of methyl. 1948, 1863, 1799, and 1737 cm^{-1} are the outer flexural vibrations of C−H on the aromatic ring. 1610, 1498, and 1461 cm^{-1} are the C═C skeleton vibration peak of the toluene aromatic ring.[46] Upon adsorption, the different vibrational bands of the toluene and air over the $BaMoO_4$ catalysts are shown in Figure 4A,B. The different peaks are obtained at (3572, 3347, 3087, 3067, 3033, 2929, 2877, 2742, 2260, 1642, 1604, 1498, 1449, 1410, 1211, 1180, and 1028) cm^{-1}. There is a negative peak found at 3608 cm^{-1} in the stretching region shown in Figure 4A.

The peak at (3067 and 3033) cm^{-1} represents C−H stretch of the phenolic groups and the bands at (3080 and 3041) cm^{-1} are assigned for the C−H stretching vibration peak on the aromatic ring of toluene in gas phase are similarly present after the adsorption also. The peaks at (1946, 1861, and 1809) cm^{-1} are the outer flexural vibration peaks of C−H on the aromatic ring missing after the adsorption of toluene over the $BaMoO_4$ catalyst. The new peaks are obtained at (1642, 1604, and 1449) cm^{-1} are denoted for the π-ring complex adsorbed over the V_2O_5−TiO_2 sample.[47,48] The peak at 1498 cm^{-1} represents the C═C skeleton vibration peak of the toluene aromatic ring. However, the bands at (2929 and 2877) cm^{-1} represents symmetric and antisymmetric stretch of $-CH_3$ attached to the aromatic ring in the gas phase toluene.[49] Therefore, during the course of adsorption, the toluene and air are mainly adsorbed as the toluene ring adsorbed with the π-ring to the catalytic site. This is presented in Scheme 1 below.

Scheme 1. Adsorption of Toluene Over the $BaMoO_4$ Catalytic Surface

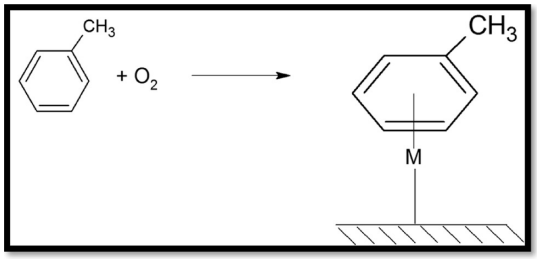

3.4.1.2. Reaction of Toluene with the $BaMoO_4$ Catalyst with Change in Temperature. Upon reaction with the $BaMoO_4$ catalyst as a function of temperature, certain new vibrational bands are formed, signifying the formation of new intermediates and some bands disappear completely, signifying the use of the surface intermediates, and similarly, the intensity of the vibrational bands varies as a function of temperature. This is portrayed in Figure 5A,B. In Figure 5A, at 50 °C post adsorption of toluene and air, the vibrational bands obtained at the stretching side are (3347, 3572, 3087, 3032, 2927, and 2828) cm^{-1}. In Figure 5B, the bands are found at (1674, 1600, 1496, 1452, 1405, 1301, 1213, and 1161) cm^{-1}. At the same time, the intensity of the bands at (2361 and 2340) cm^{-1} was obviously increased, which could be assigned to the C═O stretching vibrations of CO_2 molecules, suggesting that the toluene was completely degraded into CO_2. Among them, the bands at (3087 and 3033) cm^{-1} are attributed to phenolic C−H stretching vibration, which is characteristic of the aromatic ring. The characteristic bands of surface hydroxyls at 3572 cm^{-1} correspond to bridged−OH, and that at 3347 cm^{-1} is assigned to that of the surface −OH group, which is more labile and therefore acts as the adsorption site in the catalytic process.[50,51] The other bands (2927 and 2828) cm^{-1} represent -Me of toluene and are definitely lower in intensity, probably because -Me is oxidized as −CHO and −COOH from toluene mostly before the ring opening to mostly form the aliphatic intermediates during the reaction, as is seen at the subsequent temperatures. The bands at the bending part at 1674 cm^{-1} can be due to the stretching vibration of aldehydes, indicating the formation of benzaldehyde.[52] The bands at 1494 (shoulder) and 1600 cm^{-1} (weak) became weak after reaction and later disappeared progressively, suggesting the removal of the aromatic ring, which is observed at 50 °C with very low intensity. Similarly, the peak at 1452 cm^{-1} assigned for the π-ring adsorbed of toluene to catalysts also lowers in intensity at 50 °C, suggesting mostly the ring opening at this temperature as the other flexural bands of the aromatic ring also become very low in intensity.

1405 cm^{-1} is associated with C═O stretching vibrations of saturated aliphatic acids (formate and acetate), which could be produced by the catalytic oxidation of adsorbed toluene after ring opening.[53] The band at 1405 and 1301 cm^{-1} was mainly observed for esters over the TiO_2 (110) surface, as has been ascertained both by ab initio techniques (DFT) and experimentally by Wöll et al.[54] In the previous literature by Smith, the peak at 1300 cm^{-1} also represents the C−O stretch of esters along with a band at 1080 cm^{-1}.[55] The peaks at (1213 and 1161) cm^{-1} usually represent the C−C−O stretch of saturated aliphatic esters.[56] However, the intensity at 50 °C at these wavenumbers is low and it grows as a function of temperature, showing the formation of the esters as a function of temperature. Therefore, the peaks at (1301, 1213, and 1161) cm^{-1} all represent the ester formation post ring opening. Upon reaching 100 °C, the vibrational bands obtained in the stretching region are (weak bands at 2927, 2838, and 3032, with negative bands at 3370, 3688, and 3659) cm^{-1} and the bands at the bending region at (1761, 1717, 1692, 1678, 1635, 1593, 1495, 1460, 1404, 1304, 1232, 1158, and 1068) cm^{-1}, as shown in Figure 5A,B(d).

The weak bands at (2927, 2838, and 3032) cm^{-1} representing the −Me of toluene are present with least intensities and are almost used in the process of reaction mostly transformed to Ph-CHO and Ph-COOH. The negative bands (3370, 3688, and 3659) cm^{-1} as suggested earlier are for the usage of the surface −OH of the $BaMoO_4$ catalyst. The new peaks at (1761 and 1717) cm^{-1} are related to the formation of formation of formic acid and aldehyde post ring opening and C−C cleavage.[58] Again, there is formation of a new peak at 1692 cm^{-1}, which is primarily assigned for the stretching vibration of the aldehydes, indicating the presence of benzaldehyde.[59] The bands at (1593, 1495, and 1460) cm^{-1} (representing toluene adsorbed by π-ring) lowers further in intensity: 1402 cm^{-1} (represents aliphatic acids) and (1304, 1232, 1158, and 1068) cm^{-1} (aliphatic esters). At 150 and 200 °C, the different bands observed are same as that at 100 °C;

https://doi.org/10.1021/acsomega.4c10501
ACS Omega 2025, 10, 13080−13104

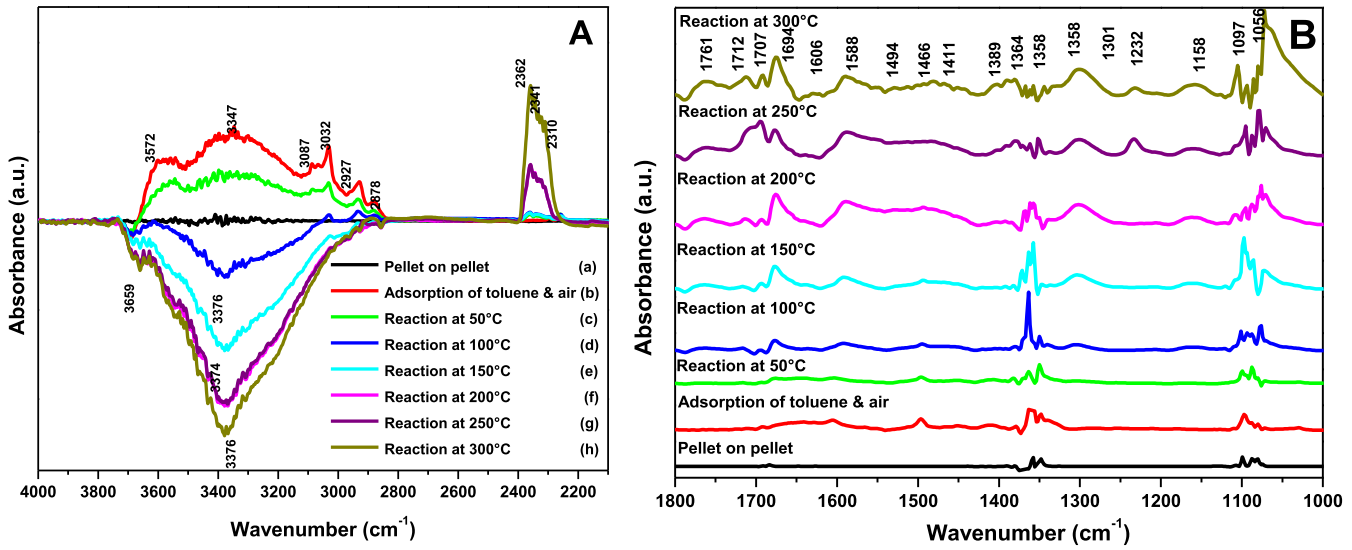

Figure 5. Adsorption and reaction of toluene and air over the $BaMoO_4$ catalyst as a function of temperature; (a) vibrational spectra for the pellet spectra taken over $BaMoO_4$ pellet as baseline; (b) adsorption at RT; (c) reaction at 50 °C; (d) reaction at 100 °C; (e) reaction at 150 °C; (f) reaction at 200 °C; (g) reaction at 250 °C; and (h) reaction at 300 °C. (A) 4000−2200 and (B) 1800−1000 cm^{-1}.

Table 2. Table Showing the Different Assignments of the FT-IR Peaks as Obtained for the Different Photocatalysts, With Different Intermediates Formed for the Process of Adsorption and the Photocatalytic Reaction[a]

intermediates on the catalytic surface	assignment	wavenumber (cm^{-1})	concerned catalytic surface	references
π-rings complex	C═C (stretch)	1610, 1498,1461, 1259, 1163 and	(BMO)-$Ad_{Air/He}$	44,45,47,48,51,53,55
	C−H (flexural vibration of aromatic)	1948, 1863, 1799, and 1737	(BMO, BWO, BMWO)-$Rxn_{Air/He}$	
	$-CH_3$(symmetrical-stretch)	2881		
benzaldehyde	>C═C<	1692 and 1672	(BWO, BMWO)-$Ad_{Air/He}$	47,48,49,54,55
	C−H− stretch		(BWO)-Rxn_{Air}, (BMWO)-Rxn_{He}	
benzoate	>C═O quinonic	1319	(BWO, BMWO)-$Ad_{Air/He}$	47,48,49,54,55
		1323	(BWO)-Rxn_{Air}, (BMWO)-$Rxn_{Air/He}$	
aliphatic aldehyde	aldehyde (>C═O)	1761, 1717, 1690, and 1707	(BMO, BWO, BMWO)-$Rxn_{Air/He}$	36,43,60
ester	>C═O bend	1300, 1080, 1213, 1161, and 1232	(BMO, BWO, BMWO)-$Rxn_{Air/He}$	36,40,43,46,49,51,60
aliphatic ester		1304, 1232, 1158, and 1068		
polymeric ester		1203		
carboxylate/acetate	>C═O bend carboxylate	1541, 1645, 1615, 1539, and 1405	(BMO, BWO, BMWO)-$Rxn_{Air/He}$	36,39,40,48,51,52,57
carbonate (bicarbonate)	C−O bend	1430 and 1393		48,49,58,59
aliphatic acid		1402, 1761, and 1705		40,45

[a]$Ad_{air/He}$ = Adsorption in air or He. $Rxn_{Ad/He}$= Reaction in air or He; BMO-$BaMoO_4$; BWO-$BaWO_4$; BMWO-$BaMo_{0.5}W_{0.5}O_4$.

there is a difference only in the intensity of these peaks to a certain extent. The peaks at (2927, 2838, 3032, and 1635) cm^{-1} are completely missing at 150 and 200 °C, showing complete utilization of these adsorbed intermediates and a strong negative band at 3370 cm^{-1}. At 275 and 300 °C certain bands are present with a very strong intensity, as in (1695, 1589, 1301, 1158, and 1232 with a shoulder at 1707) cm^{-1}.

The bands at (1695 and 1707) cm^{-1} are assigned for aliphatic aldehydes; meanwhile, the band at 1589 cm^{-1} could be attributed to the asymmetric stretching vibration of the carboxylate group from benzoic acid.[39,60] The other bands are (1301, 1158, and 1232) cm^{-1} (represents aliphatic esters) and 1707 cm^{-1} (aliphatic aldehyde), as shown in Table 2. Another significant observation is for the vibrational (2392, 2341, and 2310) cm^{-1}, which represents >C═O stretching vibrations of CO_2 molecules, showing production of the gas phase CO_2 as a function of temperature (Figure 5A) in the process of the oxidation of toluene over the $BaMoO_4$ surface. Therefore, over $BaMoO_4$, the different intermediates are benzaldehyde, benzoates, aliphatic aldehydes, aliphatic acids, and aliphatic esters, which are further oxidized to CO_2, as shown in Scheme 2 below.

3.4.1.3. Reaction Kinetics of Toluene and Air over the $BaMoO_4$ Catalyst with Time at 200 °C. The effect of toluene and air mixture oxidation at 200 °C (Figure S4) over the $BaMoO_4$ catalyst was studied to understand the amount of product CO_2 produced as a function of time. The vibrational bands in the stretching region at different temperatures (Figure S4A) show bands at (negative bands at 3688, 3663, 3372, and 3736) cm^{-1}, and they mainly represent bands for the surface ($-OH/O^{\bullet}$) groups, which are used in the due course of the reaction. The bending part of the reaction as a function of time

https://doi.org/10.1021/acsomega.4c10501
ACS Omega 2025, 10, 13080−13104

Scheme 2. Reaction of Toluene and Air Over the $BaMoO_4$ Catalytic Surface

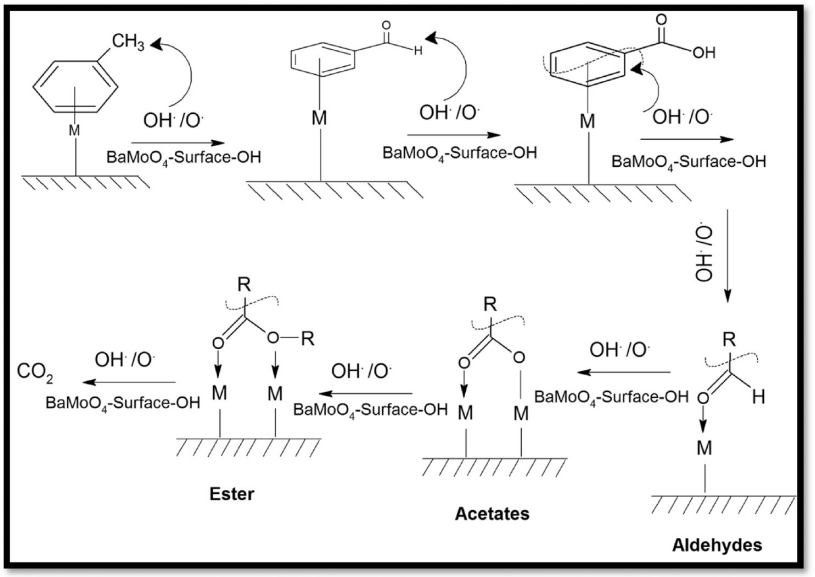

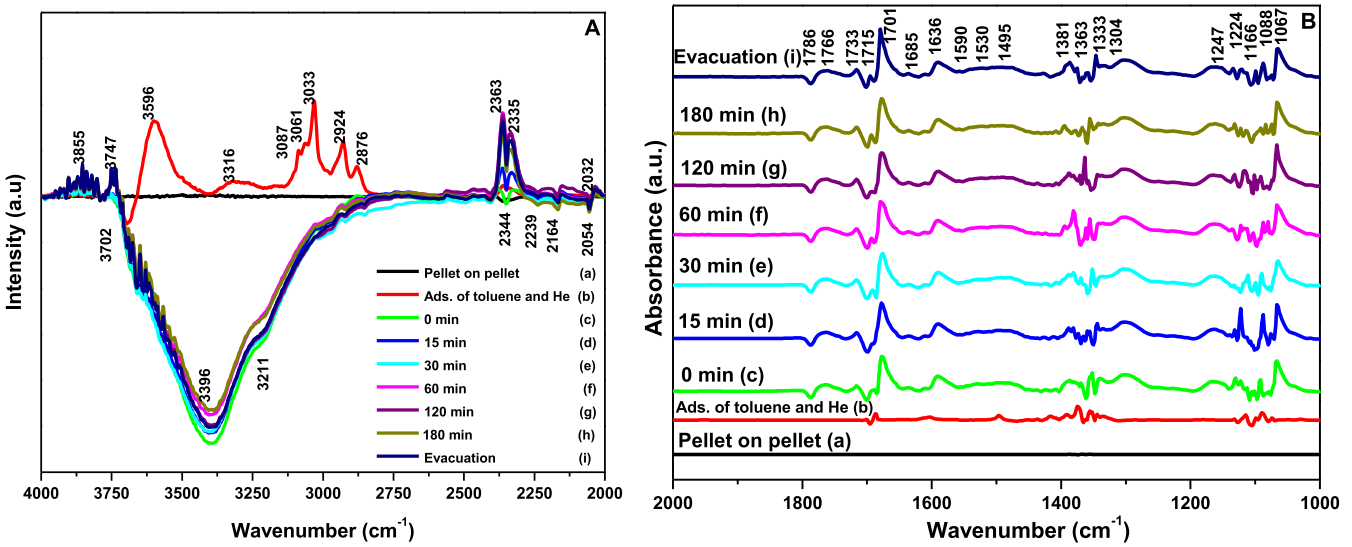

Figure 6. Adsorption and reaction of toluene and He over the $BaMoO_4$ catalyst as a function of time (at 200 °C); (a) vibrational spectra for the pellet spectra taken over $BaMoO_4$ pellet as baseline; (b) adsorption of toluene and helium at RT; (c) 0; (d) 15; (e) 30; (f) 60; (g) 120; and (h) 180 min (i) evacuation. (A) 4000−2000 and (B) 2000 −1000 cm^{-1}.

(Figure S4B) shows the presence of bands at (1761, 1707/1712, 1694, 1677, 1589, 1477, 1386, 1303, 1336, 1234, 1203, 1160, and 1112) cm^{-1}. Most of these bands are previously observed at 200 °C in the earlier section. However, there are certain new peaks observed at (1477 and 1336) cm^{-1} with a small new shoulder at 1203 cm^{-1}, and it is quite interesting to observe the different vibrational bands present after the evacuation process. The peak at 1761 cm^{-1} lowers strongly in intensity after evacuation along with the vibrational band at 1677 cm^{-1}, which is absent after evacuation and the band at 1589 cm^{-1} shifts to 1566 cm^{-1}. These observations are rationalized here.

The band at (1477 and 1336) cm^{-1} mainly represents C═O of aldehydes /acids, mostly the acid that is formed from the adsorbed aldehyde over the $BaMoO_4$ surface, which is more understood with time. The band at 1203 cm^{-1} signifies polymeric esters, which shows that with time, the esters formed may be a long chain aliphatic one resulting from the reaction of the alcohol (from aldehyde) and the acid over the $BaMoO_4$ surface. This may lead to the formation of more CO_2 as compared to oxidation from toluene only.

The bands at (1761 and 1677) cm^{-1} are absent after evacuation, showing either they are labile species or they are completely consumed before the process of evacuation. The band at 1761 cm^{-1} is for the formic acid and aldehyde post ring opening and C−C cleavage, and the band at 1677 cm^{-1} represents the benzaldehyde species. Therefore, mostly, the ring cleavage begins from the benzaldehydic stage, making the moiety not strongly adsorbed on the $BaMoO_4$ surface and the aliphatic acid, as suggested earlier, must be forming the ester over the catalytic surface, which makes this acidic species more of a labile one rather than completely adsorbed on the $BaMoO_4$ surface. The band at 1589 cm^{-1} mostly represents the π-ring bonding of the toluene over the $BaMoO_4$ surface and is

https://doi.org/10.1021/acsomega.4c10501
ACS Omega 2025, 10, 13080−13104

Scheme 3. Reaction of Toluene and He Over the $BaMoO_4$ Catalytic Surface

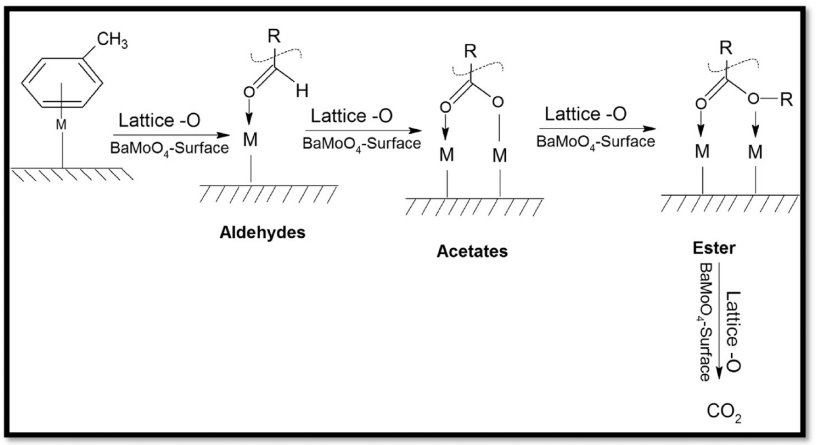

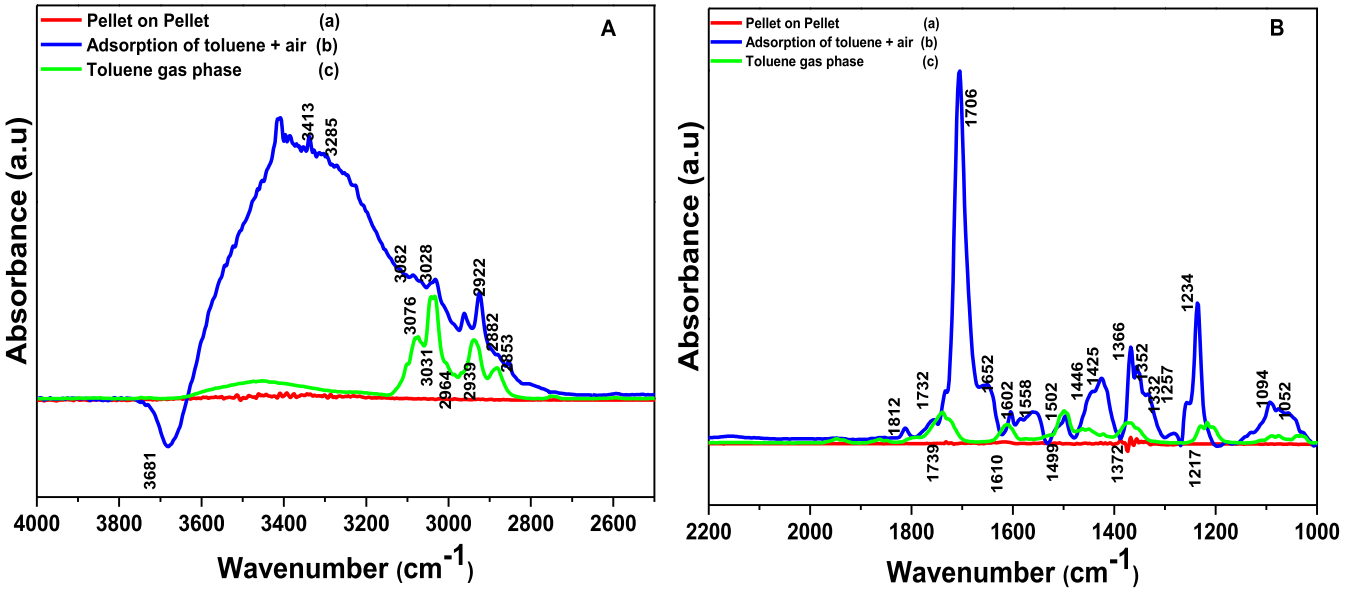

Figure 7. Adsorption of toluene and air over the $BaWO_4$ catalyst; (a) vibrational spectra for the pellet spectra taken over $BaWO_4$ pellet as baseline; (b) toluene spectra in air; and (c) toluene and air adsorbed over $BaWO_4$ surface (A) 4000−2500 and (B) 2200 −1000 cm^{-1}.

therefore not present after evacuation, as the benzene ring is cleaved during the oxidation process over the $BaMoO_4$ surface. With time, the different reaction intermediates are formed, as shown in Scheme 2, as presented earlier.

3.4.1.4. Adsorption and Reaction of Toluene with a $BaMoO_4$ Catalyst in the He Atmosphere. In order to understand the effect of lattice oxygen on the oxidation of toluene over the $BaMoO_4$ catalysts, the reaction was carried out for toluene and He mixture as a function of temperature (Figure 6). The vibrational bands were obtained in the stretching region [Figure 6A(a)]. Post adsorption of toluene and He, the vibrational bands obtained in the stretching region are (3593, 3317, 3090, 3063, 2926, 2881) cm^{-1} (Figure 6 A(a)) and the bands obtained in the bending region (Figure 6B(a)) are (1714, 1700, 1603, 1497) cm^{-1}. Here, the vibrational bands are at (3087 and 3033) cm^{-1} (attributed to phenylic C−H stretching vibration, characteristic of the aromatic ring); (2926 and 2881) cm^{-1} (represents the -Me group in the toluene aromatic ring); 1498 cm^{-1} (represents the C═C skeleton vibration peak of the toluene aromatic ring); (1700, 1717) cm^{-1} (assigned for outer flexural vibrations of C−H on the aromatic ring); and 1603 cm^{-1} (π-ring complex adsorbed over the catalyst). Therefore, in the absence of oxygen also the toluene is adsorbed over the $BaMoO_4$ surface as a π-ring complex, as is presented in Scheme 1. Therefore, in order to adsorb the toluene over the $BaMoO_4$ surface, the role of oxygen is not predominating. Reaction of toluene in the absence of air/O_2 is monitored where the different intermediates are understood as a function of temperature, as shown in Figure 6. At 100 °C, the different vibrational bands [Figure 6A,B(b)] obtained are at (1764, 1705, 1674, 1594, 1497, 1302, and 1169) cm^{-1} and two negative bands at (3381 and 1784) cm^{-1}. The negative band at 3381 cm^{-1} is due to usage of the surface −OH group of $BaMoO_4$. The new peaks at (1761 and 1705) cm^{-1} are related to the formation of formic acid and aldehyde post ring opening and C−C cleavage. The peak at 1674 cm^{-1} is primarily assigned for the stretching vibration of the aldehydes; that at 1594 cm^{-1} is attributed to the asymmetric stretching carboxylate group; and those at (1302 and 1169) cm^{-1} are as assigned for the aliphatic esters. At higher temperature 150 °C, the different vibrational bands [Figure 6A,B(c)] show almost similar bands as in 100 °C

https://doi.org/10.1021/acsomega.4c10501
ACS Omega 2025, 10, 13080−13104

Scheme 4. Adsorption of Toluene and Air Over the $BaWO_4$ Catalytic Surface

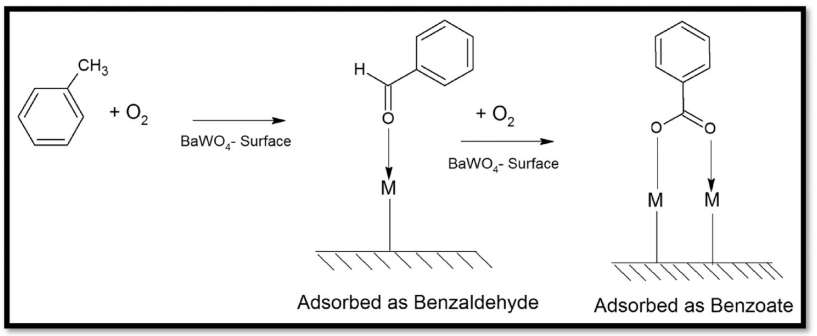

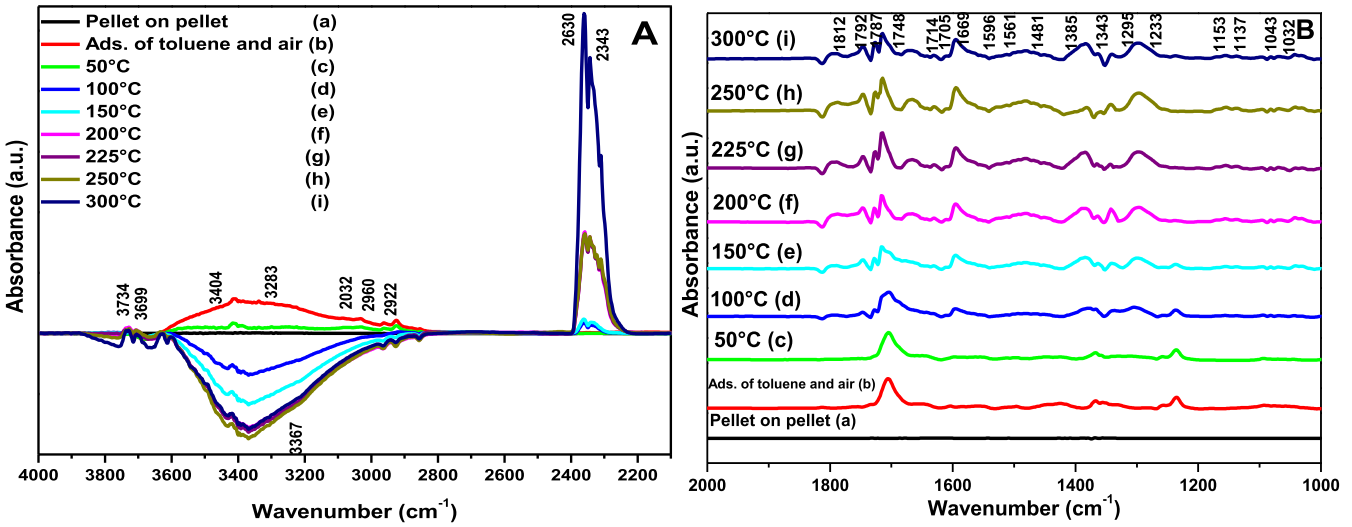

Figure 8. Reaction of toluene and air over the $BaWO_4$ catalyst within the spectral range of (A) 4000−2000 and (B) 2000 −1000 cm^{-1} as a function of temperature; (a) vibrational spectra for the pellet spectra taken over $BaWO_4$ pellet as baseline; (b) adsorption at RT; and (c) reaction at (a) 50; (b) 100; (e) 150; (f) 200; (g) 225; (h) 250; and (i) 300 °C.

except two new peaks at (1128 and 1068) cm^{-1}, a shoulder at 1334 cm^{-1}, and a new negative peak at 1701 cm^{-1}.

The bands at (1128 and 1068) cm^{-1} are also assigned to the aliphatic esters whose new presence shows further formation of these esters from some other intermediate. The shoulder at 1334 cm^{-1} is primarily assigned to the aliphatic aldehyde/acid mostly formed by using lattice oxygen from $BaMoO_4$. The negative peak at 1701 cm^{-1} (shift by 4 cm^{-1}) was correlated with formation of formates, which must now be used to form the esters, resulting in the negative peak. At further higher temperatures (200 −250) °C, the intensity of most peaks and the peak at 1334 cm^{-1} increases, pointing toward the formation of aliphatic esters. At 300 °C, there is formation of several negative peaks at (1698, 1685, 1645, 1615, 1539, 1417, 1390, 1353, 1342, 1108, and 1068) cm^{-1} along with a very small peak at (2364 and 2330) cm^{-1} representing >C═O stretch for CO_2 formation. The negative peaks of (1698 and 1685) cm^{-1} mainly correspond to formates /acetates; those at (1645, 1615, and 1539) cm^{-1} correspond to that of the carboxylates; the broad negative bands at (1417, 1390, 1353, and 1342) cm^{-1} along with the lower intensity broad negative bands (1108 and 1068) cm^{-1} correspond to aliphatic ester. Therefore, it can be well deliberated that at 300 °C, the intermediates formed over the $BaMoO_4$ surface degrade to CO_2, and as they utilize the lattice O-atom, the amount of the CO_2 formed is very meagre as compared to that of the oxidative condition. Also, the further difference with the oxidative condition is the absence of the oxidized toluene to form benzaldehyde and benzoic acid, which are mostly formed by the surface OH· and O·, which are mostly formed in the oxidative atmosphere only and not by the lattice oxygen. This is systematically shown in Scheme 3 below.

3.4.2. $BaWO_4$ Catalyst. 3.4.2.1. Adsorption of Toluene over $BaWoO_4$. Toluene and air upon adsorption on the $BaWO_4$ surface (Figure 7) behaves differently as compared to that of the earlier $BaMoO_4$ surface. This can be well evidenced as the different bands that are obtained are (3413, 3285, 3082, 3028, 2964, 2922, and 2853) cm^{-1} in the stretching region [Figure 7A(c)] with a negative band at 3681 cm^{-1} and (1812, 1732, 1706, 1662, 1652, 1604, 1568, 1502, 1446, 1425, 1360, 1352, 1332, 1234, 1097, and 1052) cm^{-1} in the bending region [Figure 7B(c)].

The new bands are obtained at (1706, 1558, 1446, 1425, 1366, 1352, 1332, and 1234) cm^{-1} feature in the bending region. The negative band at 3681 cm^{-1} represents the surface −OH group used in the adsorption process. The peak at (3082, 3028) cm^{-1} represents the C−H stretch of the Phenylic groups. The strong band at 1702 cm^{-1} is assigned for the C═O stretch of the adsorbed benzaldehyde,[61] and the vibrational band at 1558 cm^{-1} is for the asymmetric C−O stretching vibration of the benzoate.[47,62] The shoulders at (1662, 1652, 1604) cm^{-1} represent C═O stretching vibration of the

https://doi.org/10.1021/acsomega.4c10501
ACS Omega 2025, 10, 13080−13104

Scheme 5. Reaction of Toluene and Air Over the $BaWO_4$ Catalytic Surface

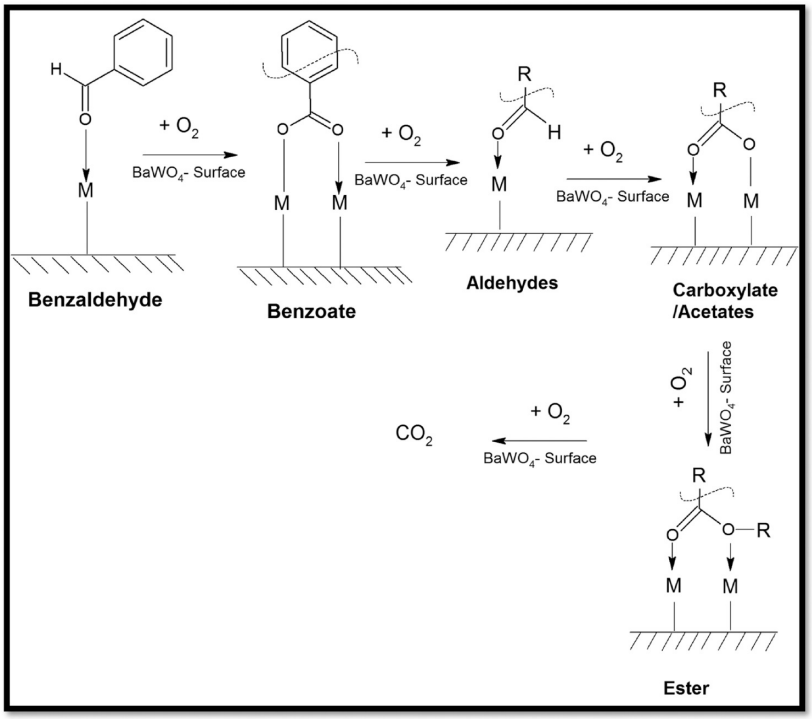

adsorbed benzaldehyde from the toluene;[48] and the peak at 1332 cm^{-1} represents the skeletal C−C vibration for the benzaldehyde.[63] The peak around 1446 cm^{-1} represents the C−C stretching for the aromatic ring in the aromatic aldehydes.[64] The vibrational band around 1425 cm^{-1} represents the symmetric C−O stretching vibration for the benzoates.[47] The other bands at (1232, 1097, and 1052) cm^{-1} represent that of the benzoates.[55,65,66] At this juncture, it should be noted that the vibrational bands (2964, 2922, and 2853) cm^{-1} represent C−H stretch for the whether -Me for toluene and will be same for C−H stretch for the Ph-CHO or Ph-COOH and therefore do not show the presence of Ph-CH_3 further even after adsorption.

Therefore, on the $BaWO_4$ surface, the toluene and air are adsorbed together as benzaldehyde and benzoate. The role of air/O_2 will be further elucidated during the adsorption of toluene in He over the BaWO4 surface. The adsorption of toluene and air is summarized in Scheme 4 above. At this stage, now it is quite intriguing to understand the reason that triggers such a process of adsorption over the $BaWO_4$ surface under ambient conditions, whereas in $BaMoO_4$, the process of adsorption is merely Ph-CH_3 adsorbed over the surface by the π-electron concentration attached to the $BaMoO_4$ (mainly Mo). This would be further probed while understanding the XPS and the ab initio results in a far atomistic microscopic way. Also, the primary role of the O_2/air will also be envisaged properly once the adsorption of Ph-CH_3 over $BaWO_4$ is understood in the absence of O_2.

3.4.2.2. Reaction of Toluene and Air over the $BaWO_4$ Catalyst with Change in Temperature. The oxidation of toluene and air over the $BaWO_4$ surface is presented in Figure 8. At 50 °C, the stretching region [Figure 8A(b)] shows different vibrational bands formed by the oxidation process at (3409, 3377, 3032, and 2922) cm^{-1}, and the bands found in the bending region [Figure 8B(b)] are at (1705, 1595, 1562, 1449, 1420, 1367, 1307, and 1233) cm^{-1}. The bands obtained at 50 °C are almost similar to those obtained in the adsorption of the toluene and air over the $BaWO_4$ catalyst. The new bands that are observed are at 1595 cm^{-1} and at 1308 cm^{-1}. The band at 1595 cm^{-1} is attributed to the asymmetric stretching carboxylate group, similar to that of the benzoate group; at 1308 cm^{-1}, in the previous literature by Smith, the peak at 1300 cm^{-1} also represents the C−O stretch of esters along with a band at 1080 cm^{-1}. Therefore, it implies that at 50 °C, more of the benzaldehyde is converted to benzoate and there is formation of ester by the recombination of the two. At 100 °C, there are negative peaks at (3032, 2960, and 2922) cm^{-1} in the stretch region [Figure 8A(d)] and the bending region shows peaks at (1747, 1716, 1669, 1597, 1556, 1480, 1454, 1373, 1303, 1234, and 1153) cm^{-1}, with a new shoulder observed at 1363 cm^{-1} [Figure 8B(d)]. The sharp and strong peak at 1717 cm^{-1} is related to the formation of formation of formic acid and aldehyde post ring opening and C−C cleavage[36] and the peak at 1747 cm^{-1} are the outer flexural vibrations of C−H on the aromatic ring.

Therefore, together they decipher the fact that the aromatic ring to the benzaldehyde opens to form formic acid of the aliphatic aldehyde. The band at 1662 cm^{-1} (represents the adsorbed benzaldehyde; with a shift of 7 cm^{-1}) lowers in intensity, showing use of them; post reaction, −1594 cm^{-1} is attributed to the asymmetric stretching carboxylate group and not adsorbed toluene; vibrational band at 1558 cm^{-1} is for the asymmetric C−O stretching vibration of the benzoate;[48,49] bands at (1480 and 1363) cm^{-1} mainly represent C═O of aldehydes /acids, mostly the acid that is formed from the adsorbed aldehyde over the $BaWO_4$ surface, which is more understood with time; the peak around 1454 cm^{-1} represents the C−C stretching for the aromatic ring in the aromatic aldehydes;[50] the band at (1373, 1301, 1234, and 1153) cm^{-1} was mainly observed for esters over the TiO_2 (110) surface, as

https://doi.org/10.1021/acsomega.4c10501
ACS Omega 2025, 10, 13080−13104

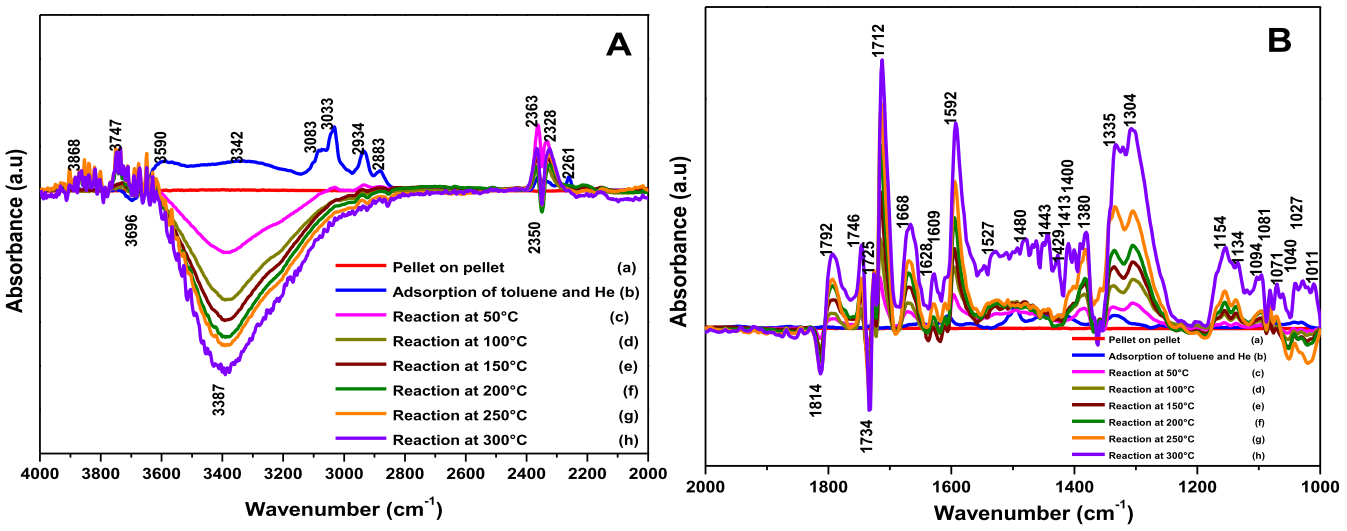

Figure 9. Adsorption and reaction of toluene and He over the $BaWO_4$ catalyst as a function of temperature; (a) vibrational spectra for the pellet spectra taken over $BaWO_4$ pellet as baseline; (b) adsorption at RT; (c) reaction at 50 °C; (d) reaction at 100 °C; (e) reaction at 150 °C; (f) reaction at 200 °C; (g) reaction at 250 °C; and (h) reaction at 300 °C. (A) 4000−2000 and (B) 2000 −1000 cm^{-1}.

has been ascertained both by ab initio techniques (DFT) and experimentally by Woll et al.[54] The peaks (2364 and 2330) cm^{-1} representing >C═O stretch for CO_2 formation start from 100 °C. At 150 °C, several new bands are formed at the bending part of the spectra [Figure 8B(e)] (1793, 1753, 1714, 1669, 1598, 1562, 1480, 1383, 1364, 1295, 1233, 1153, 1137, and 1032) cm^{-1}. Out of these, mainly the peaks at (1793, 1383, 1295, 1233, 1137, and 1032) cm^{-1} are seen for the first time for the $BaWO_4$ surface. The band around after reaction for the 1793 cm^{-1} is related to C═O stretching vibration, which is the characteristic of aldehyde, esters, or carboxylic acid species.

The band at 1669 cm^{-1} is associated to the stretching vibration of the aldehydes, giving the evidence for the formation of benzaldehyde;[38] the band at 1383 cm^{-1} is associated to the symmetric stretching ν(OCO) group for the esters observed mainly over $ZnAl_2O_4$ catalysts for thermal oxidation of toluene;[67] the band at 1295 cm^{-1} was mainly observed for esters over the TiO_2 (110) surface, as has been ascertained both by ab initio techniques (DFT) and experimentally by Woll et al.[40] Bands at (1233, 1137, and 1032) cm^{-1} are also assigned for the aliphatic esters, showing further formation of these esters. The bands representing CO_2 (2364 and 2330) cm^{-1} increase in intensity as compared to 100 °C [Figure 8A(e)]. The other bands are almost the same as observed at 100 °C thereby, showing mostly the formation of the aliphatic aldehydes and aliphatic esters, which finally form CO_2. The bands at a higher temperature of 200 °C and the bands obtained at further higher temperatures [Figure 8B(f)] are similar to the bands obtained at 150 °C; however, the peaks representing the CO_2 increase in intensity, showing further gas phase formation of the CO_2 as complete mineralization product of toluene and air over the $BaWO_4$ catalyst. The reaction mechanism is portrayed in Scheme 5.

3.4.2.3. Reaction Kinetics of Toluene and Air over the $BaWO_4$ Catalyst with Time at 200 °C. The effect of toluene and air mixture oxidation at 200 °C (Figure S5) over the $BaWO_4$ catalyst was studied as a function of time to understand the amount of product CO_2 produced as a function of time. The vibrational bands in the stretching region at different temperature (Figure S5A) show bands at (negative bands at 3386, 2962, 2927, and 2828) cm^{-1}, and they mainly represent bands for the surface (−OH/O•) and the peak at (2962 and 2927) cm^{-1} represents C−H stretch of the phenylic groups. The bending part of the reaction as a function of time (Figure S5B) shows the presence of bands at (1788, 1744, 1724, 1716, 1669, 1612, 1597, 1497, 1380, 1368, 1306, 1257, 1155, 1137, 1098, and 1045) cm^{-1}. Most of these bands are previously observed at 200 °C in the earlier section. However, there are certain new peaks observed at (1497 and 1368) cm^{-1}, and there are no new peaks observed after evacuation. These observations are rationalized here.

The bands present at (1497 and 1363) cm^{-1} mainly represent C═O of aldehydes /acids, mostly the acid that is formed from the adsorbed aldehyde over the $BaWO_4$ surface, which is more understood with time; the peak around 1454 cm^{-1} represents the C−C stretching for the aromatic ring in the aromatic aldehydes.[50] Therefore, with the kinetics, the aldehydes as intermediates are formed more. However, the striking feature for the kinetics study is the formation of CO_2 as a function of time (Figure S5A), which shows complete mineralization of toluene over the $BaWO_4$ surface effectively with release of CO_2. The other bands present are almost the same as compared to the thermal effect, as discussed earlier, and thereby mostly follow the Scheme 5 as shown above.

3.4.2.4. Adsorption and Reaction of Toluene and He over the $BaWO_4$ Surface. Upon adsorption of toluene in the presence of He/or absence of oxygen [Figure 9(b)A,B], mainly the vibrational bands stretch region [Figure 9A(b)] obtained are at (3590, 3342, 3083, 3033, 2934, and 2883) cm^{-1} and in the bending part as (1642, 1599, 1556, 1496, 1450, 1415, and 1332) cm^{-1}, as shown in Figure 9B(b).

The new peaks are obtained at (1642, 1599, and 1450) cm^{-1} and are denoted for the π-ring complex adsorbed over the V_2O_5−TiO_2 sample; the peak at 1496 cm^{-1} represents the C═C skeleton vibration peak of the toluene aromatic ring; bands at (2934 and 2883) cm^{-1} represent symmetric and antisymmetric stretch of $-CH_3$ attached to the aromatic ring in the gas phase toluene. Now, the intensity of the peaks 1415 and 1332 cm^{-1} is quite low as compared to the others. The

https://doi.org/10.1021/acsomega.4c10501
ACS Omega 2025, 10, 13080−13104

Scheme 6. Reaction of Toluene and He Over the $BaWO_4$ Catalytic Surface

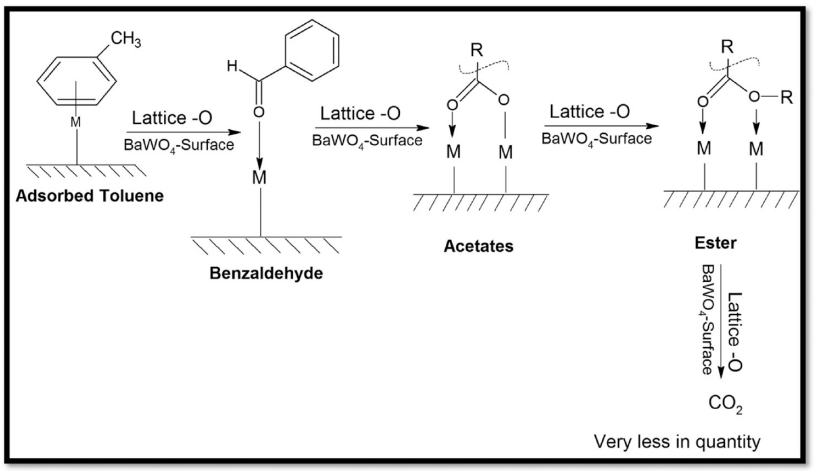

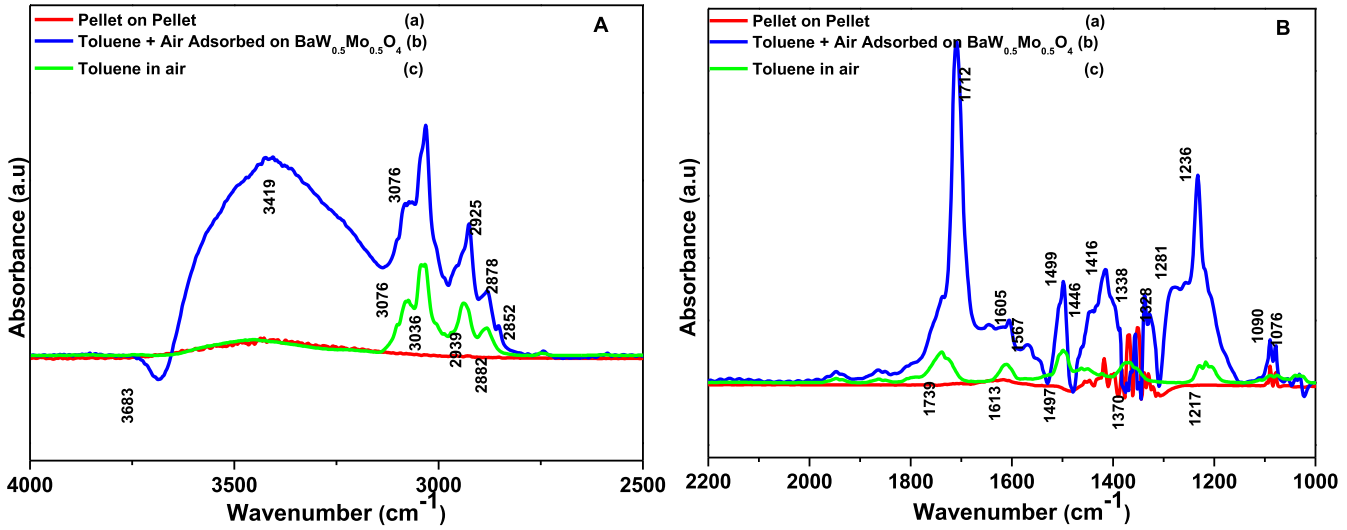

Figure 10. Adsorption of toluene and air over the $BaW_{0.5}Mo_{0.5}O_4$ catalyst; (a) vibrational spectra for the pellet spectra taken over $BaW_{0.5}Mo_{0.5}O_4$ pellet as baseline; (b) toluene spectra in air; (c) toluene and air adsorbed over the $BaW_{0.5}Mo_{0.5}O_4$ surface. (A) 4000−2500 and (B) 2200 −1000 cm^{-1}.

peak at (1414 and 1332) cm^{-1} represents aldehydes, which are mostly benzaldehyde here; however, the other vibrational bands representing benzaldehyde are absent. The formation of benzaldehyde even if formed is very negligible as compared to that in the oxidative condition. Therefore, in the absence of oxygen, the toluene is mainly adsorbed by the π-ring of the aromatic phenyl ring without the $-CH_3$ group, as represented in Scheme 1 previously. Therefore, it is clear that in $BaWO_4$ catalysts, the adsorbed oxygen is required for the adsorbed moieties of benzaldehyde and benzoate, as observed in Scheme 4.

Upon reaction at 100 °C, there are definite bands that are obtained in the stretching region [Figure 9A(c)] with negative bands at (3383, 2363, and 2338) cm^{-1} and in the bending region [Figure 9B(c)] (1814 and 1734) cm^{-1}. Apart from that, the bending region also possesses the vibrational bands at [1761, 1716, 1671, 1634, 1594, 1496, and 1380 and doublet at (1337 and 1303) and (1155 and 1134)] cm^{-1}. The peak at (1761 and 1717) cm^{-1} is related to the formation of formic acid and aldehyde post ring opening and C−C cleavage.[36] Again there is formation of a new peak at 1692 cm^{-1}, which is primarily assigned to the stretching vibration of the aldehydes, indicating the presence of benzaldehyde.[45] The bands at (1593 and 1495) cm^{-1} (representing Toluene adsorbed by π-ring) lower further in intensity. The band at 1383 cm^{-1} is associated to the symmetric stretching v(OCO) group for the esters observed mainly over $ZnAl_2O_4$ catalysts for thermal oxidation of toluene.[51] The doublet (1336 and 1303) cm^{-1} mainly represents C═O of aldehydes /acids mostly the acid that is formed from the adsorbed aldehyde over the $BaWO_4$ surface in the presence of He. The next doublet (1158 and 1068) cm^{-1} depicts aliphatic esters. The bands (2363 and 2328) cm^{-1} representing gaseous CO_2 are also obtained at 100 °C, indicating mineralization of toluene to a certain extent. Therefore, at 100 °C, the adsorbed toluene is converted to benzaldehyde, which in turn is converted to aliphatic ester and is converted to CO_2 with the help of the lattice oxygen present in $BaWO_4$.

At 150 °C, similarly, the vibrational bands are obtained at [1792, 1746, 1671, 1630, 1598, 1500, and 1382 with doublet at (1335 and 1305) and (1134, 1094)] cm^{-1} [Figure 9B(e)] along with the similar negative bands and the similar bands observed in the stretching region. Here the new band is observed at 1792 cm^{-1} is related to >C═O stretching

https://doi.org/10.1021/acsomega.4c10501
ACS Omega 2025, 10, 13080−13104

Scheme 7. Adsorption of Toluene and Air Over the $BaMo_{0.5}W_{0.5}O_4$ Catalytic Surface

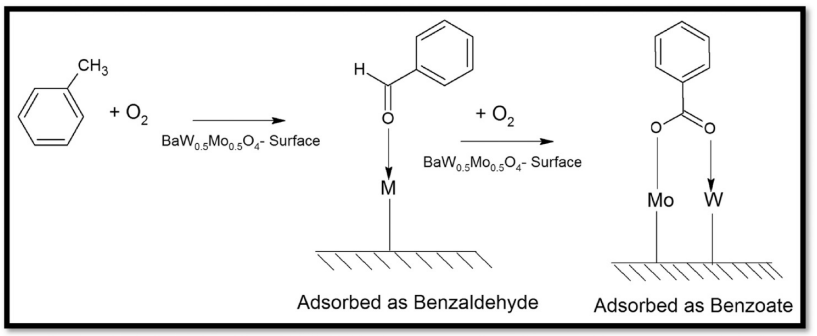

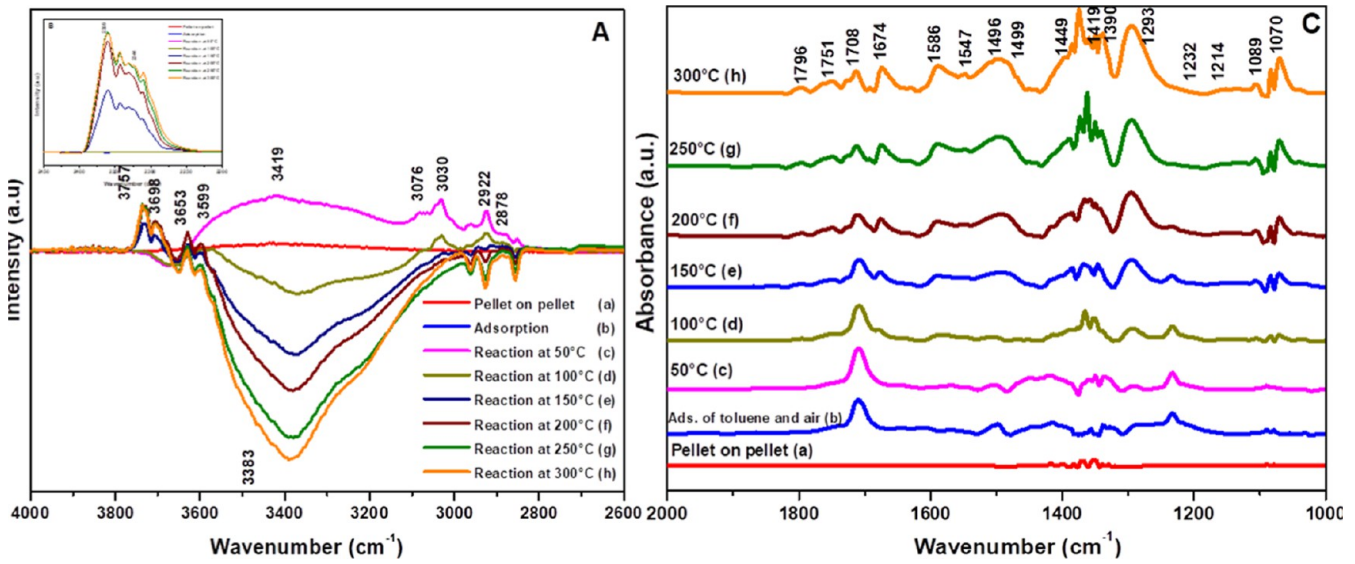

Figure 11. Adsorption and reaction of toluene and air over the $BaW_{0.5}Mo_{0.5}O_4$ catalyst as a function of temperature; (a) vibrational spectra for the pellet spectra taken $BaW_{0.5}Mo_{0.5}O_4$ pellet as baseline; (b) adsorption at RT; (c) reaction at 50 °C; (d) reaction at 100 °C; (e) reaction at 150 °C; (f) reaction at 200 °C; (g) reaction at 250 °C; and (h) reaction at 300 °C. (A) 4000−2600, (B) 2450−2200, and (C) 2000−1000 cm^{-1}.

vibration, which is the characteristic of aldehyde, esters, or carboxylic acid species; the other bands are same as at 100 °C; only their intensities are different.

At higher temperatures (250 and 300) °C, almost similar bands are obtained, as has been obtained here. However, at 300 °C, there is a new doublet obtained at (1430 and 1393) cm^{-1} and at (1389 and 1384) cm^{-1}. The peak at (1430 and 1393) cm^{-1} is assigned to the bicarbonate type species for CO_2 adsorption over TiO_2 nanotubes;[68,69] the 1393 cm^{-1} band is associated to the symmetric stretching v(OCO) group for aliphatic carboxylic acid species, which forms doublet (1389 and 1384) cm^{-1}, showing mostly two types of carboxylates present.[38] Therefore, with He though, a small amount of CO_2 is produced; it lowers down with temperature, which may be indicative of the fact that lattice O− is not replenished in the absence of oxygen, thereby lowering the formation of the CO_2; however, the carboxylates and aliphatic esters are definitely formed as intermediates. The above intermediates effectively forming a much less amount of CO_2 are mechanistically represented in Scheme 6.

3.4.3. $BaMo_{0.5}W_{0.5}O_4$—Catalyst. 3.4.3.1. Adsorption of Toluene over $BaMo_{0.5}W_{0.5}O_4$. Toluene and air upon adsorption on the $BaMo_{0.5}W_{0.5}O_4$ surface (Figure 10) behave almost similarly as that of the $BaWO_4$ surface. This can be well evidenced as the different bands that are obtained are (3419, 3076, 3036, 2922, 2878, and 2852) cm^{-1} in the stretching region [Figure 10A(c)] with a negative band at 3681 cm^{-1} and (1712, 1652, 1605, 1568, 1499, 1446, 1425, 1360, 1352, 1332, 1234, 1097, and 1052) cm^{-1} in the bending region [Figure 10B(c)]. The negative band 3681 cm^{-1} represents the surface −OH group used in the adsorption process. The peak at (3082 and 3028) cm^{-1} represents the C−H stretch of the phenylic groups. The strong band at 1712 cm^{-1} is assigned for the C═O stretch of the adsorbed benzaldehyde;[47,48] the vibrational band at 1567 cm^{-1} is for the asymmetric C−O stretching vibration of the benzoate.[48,65] The shoulders at (1662 and 1605) cm^{-1} are C═O stretching vibration of the aromatic aldehydic adsorbate, mostly here, benzaldehyde is adsorbed from toluene;[48,49,65] and the peak at 1338 cm^{-1} represents the skeletal C−C vibration for the benzaldehyde, and the peak around 1446 cm^{-1} represents the C−C stretching for the aromatic ring in the aromatic aldehydes.[50]

The vibrational band around 1416 cm^{-1} represents the symmetric C−O stretching vibration for benzoates.[47] The other bands at (1236, 1090, and 1052) cm^{-1} represent that of the benzoates.

However, there are no strong bands representing the Ph-CH_3 adsorption over $BaMo_{0.5}W_{0.5}O_4$ surface with aromatic π-bond as observed for the $BaMoO_4$ catalyst. At this juncture, it should be clarified that the vibrational bands (2964, 2922,

https://doi.org/10.1021/acsomega.4c10501
ACS Omega 2025, 10, 13080−13104

Scheme 8. Reaction of Toluene and Air Over the $BaMo_{0.5}W_{0.5}O_4$ Catalytic Surface

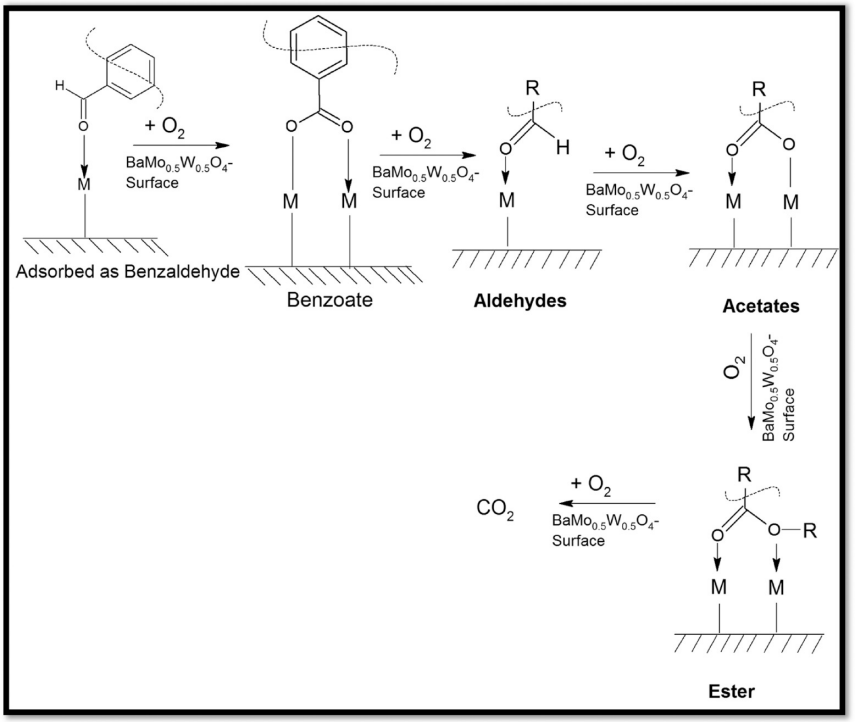

2853) cm^{-1} represent C−H stretch for Me. Whether Me is attached as Ph-CH_3 or Ph-CHO or Ph-COOH, it will be similar. Therefore, it does not conclude presence of Ph-CH_3 further even after adsorption. However, as compared to that of the $BaWO_4$ catalyst, there is a definite shift in the band values, as obtained for the $BaMo_{0.5}W_{0.5}O_4$ catalyst, which essentially shows that the intermediates are not exactly bonded to W only but are bonded simultaneously to W and Mo, which will be better understood in the XPS understanding part. The above understanding is reflected in Scheme 7.

3.4.3.2. Reaction of Toluene and Air over the $BaWO_4$ Catalyst with Change in Temperature. The oxidation of toluene and air over the $BaMo_{0.5}W_{0.5}O_4$ surface is presented in Figure 11. At 50 °C, the stretching region [Figure 11A(b)] shows different vibrational bands formed by the oxidation process at (3675, 3419, 3077, 3031, 2962, 2924, and 2878) cm^{-1} and the bands found in the bending region [Figure 11B(b)] are at (1796, 1751, 1708, 1678, 1570, 1541, 1502, 1449, 1420, 1367, 1350, 1288, 1234, and 1070) cm^{-1}. Post adsorption in the stretching region, the intensity of the bands 3419 cm^{-1} representing the −OH group and other (3675, 3077, 3031, 2962, 2924, and 2878) cm^{-1}, referring to the adsorbed toluene as benzaldehyde and benzoate, reduces to a large extent, showing that the different intermediates are formed from these adsorbed species, and there are certain definite new peaks that are obtained (1796, 1751, 1678, 1541, 1367, 1350, and 1070) cm^{-1}. As observed earlier, the band after reaction at (1796 and 1751) cm^{-1} is related to C═O stretching vibration, which is the characteristic of aldehyde, esters, or carboxylic acid species;[36,70] the band at 1678 cm^{-1} is assigned to the stretching vibration of the aldehydes, indicating the presence of aliphatic aldehydes;[45] the low intensity bands formed at (1367 and 1350) cm^{-1} represent aliphatic esters, as is discussed earlier; the bands at (1541 and 1070) cm^{-1} represent >C═O of benzoate or aliphatic acids. However, post reaction, it is more probable to think about the formation of the aliphatic acetates as compared to benzoates. This will be more clear at higher temperatures. The reaction temperature at 100 °C resulted in different bands obtained for oxidation of toluene and air [Figure 11A(d)] in the stretching region 3419 cm^{-1}, which shows a negative intensity, whereas the intensities for the bands (3675, 3077, 3031, 2962, 2924, and 2878) cm^{-1}, referring to the adsorbed toluene as benzaldehyde and benzoate, reduce to a large extent. Bands appear at the bending region [Figure 11B(d)] (1796, 1751, 1708, 1678, 1590, 1545, 1504, 1449, 1388, 1364, 1358, 1293, 1234, 1162, and 1071) cm^{-1}. Most of these bands were present at 50 °C, with the exception of the bands at (1590, 1388, and 1162) cm^{-1}. Before explaining the new bands, let us revisit the bands at (1541 and 1070) cm^{-1}, which either represents >C═O for benzoate or aliphatic acetates. The intensity of this band increases at 100 °C, showing the formation of new species. However, the other bands (1567, 1416, 1236, 1098, and 1056) cm^{-1} are either absent or have lowered considerably in intensity.

Therefore, it is quite clear that the benzoate intermediate is converted to some new intermediate like aliphatic acetate by ring opening, which now represents these two peaks (1541 and 1070) cm^{-1}. Similarly, the new peak 1594 cm^{-1} is attributed to the asymmetric stretching carboxylate group in the present scenario and not to π-ring adsorbed toluene; the band at 1383 cm^{-1} is associated to the symmetric stretching ν(OCO) group for the esters observed mainly over $ZnAl_2O_4$, as has been previously observed over the $BaWO_4$ surface.[51] The band at 1293 cm^{-1} was mainly observed for esters over the TiO_2 (110) surface, as has been ascertained both by ab initio techniques (DFT) and experimentally by Woll et al.;[40] and the peak at 1161 cm^{-1} usually represents the C−C−O stretch of saturated aliphatic esters as observed over the $BaMoO_4$ surface.[43] Apart from this, there is a systematic lowering in intensity of the band

https://doi.org/10.1021/acsomega.4c10501
ACS Omega 2025, 10, 13080−13104

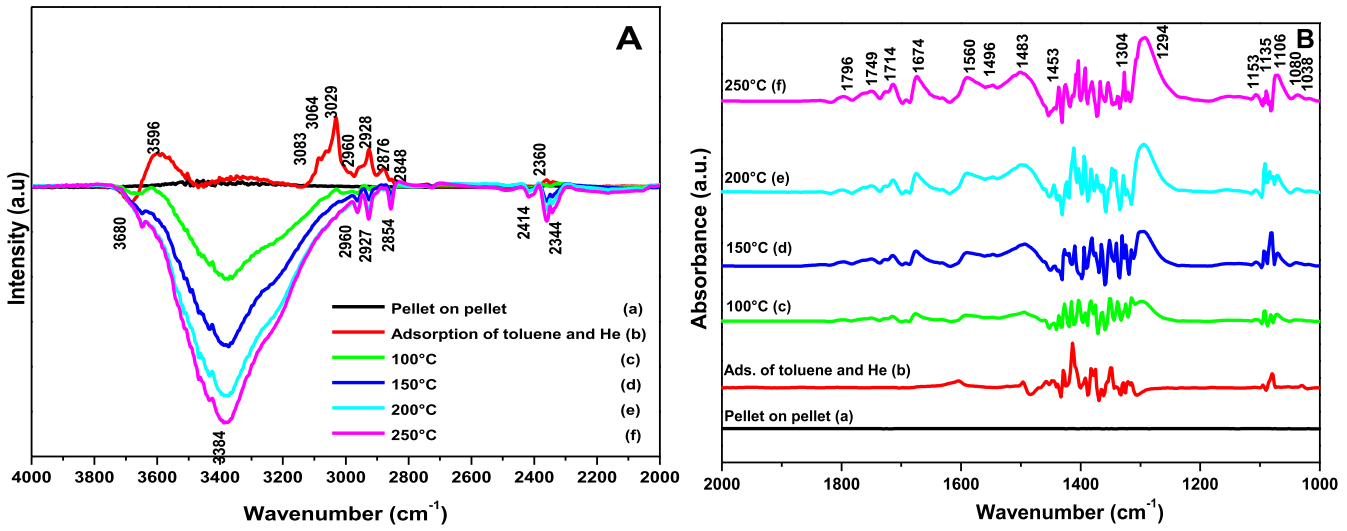

Figure 12. Adsorption and reaction of toluene and He over the $BaW_{0.5}Mo_{0.5}O_4$ catalyst as a function of temperature; (a) vibrational spectra for the pellet spectra taken $BaW_{0.5}Mo_{0.5}O_4$ pellet as baseline; (b) adsorption at RT; (c) reaction at 100 °C; (d) reaction at 150 °C; (e) reaction at 200 °C; and (f) reaction at 250 °C. (A) 4000−2000 and (B) 2000 −1000 cm^{-1}.

at 1708 cm^{-1} (representing benzaldehyde/aliphatic aldehyde); (1504 and 1459) cm^{-1} (both representing mostly benzaldehyde). There is systematic growth in the intensity of the bands at (1591, 1293, 1071, and 1162) cm^{-1}. At 150 °C, the stretch region shows bands at [doublet (3757 and 3698) and (3653 and 3599)] cm^{-1} [Figure 11A(e)] and the prominent negative bands at (3375, 3076, 3030, 2926, and 2852) cm^{-1}. The initial doublets are due to C−O stretch bands of gas phase CO_2. The bending bands are obtained at (1796, 1750, 1675, 1589, 1492, 1385, 1367, 1347, 1293, 1231, 1155, 1137, and 1069) cm^{-1} [Figure 11B(e)] along with (2392, 2341, and 2310) cm^{-1}, which represent C═O stretching vibrations of CO_2 molecules, showing production of the gas phase CO_2 as a function of temperature in the (Figure 11A inset). In the vibrational part, new bands are obtained at (1155 and 1137) cm^{-1}, and there is a systematic alteration in the intensity of the bands.

The bands at (1155 and 1137) cm^{-1} represent the aliphatic esters, as has been observed earlier over the $BaMoO_4$ surface, and the band is absent at 1449 cm^{-1}. At 200 °C and higher, the same bands are obtained but with different intensities. The intensity of the gaseous CO_2 formed increases with temperature, as can be observed in the inset of Figure 11A, and the intensities of [doublet (3757 and 3698) and (3653 and 3599)] cm^{-1} are increased. This complete understanding is reflected in Scheme 8.

3.4.3.3. Reaction Kinetics of Toluene−Air over the $BaMo_{0.5}W_{0.5}O_4$ Catalyst with Time at 200 °C. The effect of toluene and air mixture oxidation at 150 °C (Figure S6) over the $BaMo_{0.5}W_{0.5}O_4$ catalyst was studied as a function of time to understand the amount of product CO_2 produced as a function of time. The vibrational bands in the stretching region at different temperatures (Figure S6A) show bands at (negative bands at 3375, 3076, 3030, 2927, and 2852) cm^{-1}, and they mainly represent bands for the surface (−OH/$O^{\bullet}$) and the peak at (3030 and 2927) cm^{-1} represents C−H stretch of the phenolic groups. The bending part of the reaction as a function of time (Figure S6B) shows the presence of bands at (1796, 1754, 1675, 1589, 1513, 1492, 1385, 1367, 1347, 1231, 1155, 1137, and 1064) cm^{-1}. Most of these bands are previously observed at 150 °C in the earlier section. However, there are certain new peaks observed at (1714 and 1513) cm^{-1}, and no new peaks observed after evacuation. The new peak at 1714 cm^{-1} along with that at 1754 cm^{-1} are related to the formation of formation of formic acid and aldehyde post ring opening and C−C cleavage;[36] and 1513 cm^{-1} represents that of the carboxylates. This shows that these intermediates are formed in more with time, which are finally oxidized to CO_2. The amount of CO_2 increases as a function of time, as has been shown in the inset of Figure 11. A. However, there are no new species formed; therefore, it follows Scheme 8 only.

3.4.3.4. Adsorption and Reaction of Toluene−He over the $BaMo_{0.5}W_{0.5}O_4$ Surface. The adsorption and reaction of toluene and He over the $BaMo_{0.5}W_{0.5}O_4$ catalyst surface is shown in Figure 12A,B. Post adsorption of toluene and He, the bands were obtained in the stretch region [Figure 12A(c)] (3596, 3086, 3064, 3029, 2960, 2928, and 2848) cm^{-1} and the bands in the bending region are (1609, 1498, 1455, 1080, and 1030) cm^{-1} [Figure 12B(c)]. The peak at (3086 and 3033) cm^{-1} represents C−H stretch of the phenolic groups, and the bands at (3080 and 3064) cm^{-1} are assigned for the C−H stretching vibration peak on the aromatic ring of toluene in gas phase, which are similarly present after the adsorption also; vibrational bands (2960, 2928, and 2848) cm^{-1} represent C−H stretch for the whether -Me for toluene; bands at (1604 and 1449) cm^{-1} are denoted for the π-ring complex adsorbed over the V_2O_5−TiO_2 sample.[33,34] The peak at 1498 cm^{-1} represents the >C═C< skeleton vibration peak of the toluene aromatic ring; 1455 cm^{-1} is assigned for the π-ring adsorbed of toluene. Therefore, the toluene in the absence of air over the $BaMo_{0.5}W_{0.5}O_4$ surface is adsorbed as a π-ring complex, as in the $BaMoO_4/BaWO_4$ surface, as shown in Scheme-1 previously.

At 100 °C, different vibrational peaks are obtained at (3400, 3086, 2960, 2928, and 2848) cm^{-1} as mainly negative peaks [Figure 12A(d)] and in the bending region [Figure 12B(d)] (1797, 1750, 1711, 1673, 1590, 1548, 1510, 1480, 1461, 1298, 1147, 1137, 1073, 1032, and 1016) cm^{-1}. Bands at (1799) cm^{-1} represent outer flexural vibrations of C−H on the aromatic ring; peaks at (1750 and 1711) cm^{-1} are related to the formation of formic acid and aldehyde post ring opening

https://doi.org/10.1021/acsomega.4c10501
ACS Omega 2025, 10, 13080−13104

Scheme 9. Adsorption and Reaction of Toluene−He Over the $BaMo_{0.5}W_{0.5}O_4$ Catalytic Surface

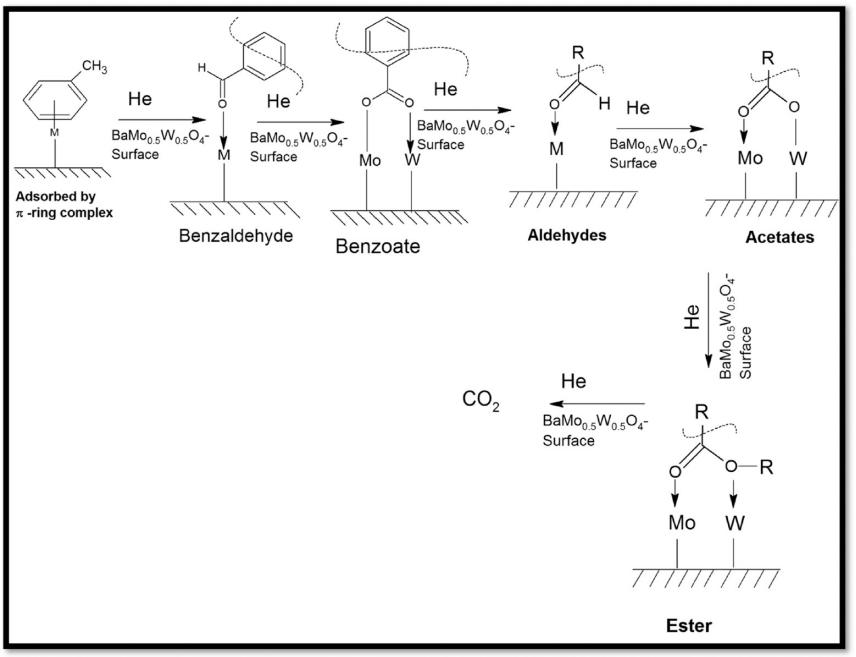

and C−C cleavage;[36] the bands at 1674 cm^{-1} (stretching vibration of aldehydes, indicating the formation of benzaldehyde); 1590 cm^{-1} (asymmetric stretching vibration of the carboxylate group from benzoic acid); (1548 and 1070) cm^{-1} (represents >C═O of benzoate or aliphatic acids); 1510 cm^{-1} (represents carboxylates); (1498 and 1461) cm^{-1} (>C═C skeleton vibration peak of the toluene aromatic ring); and 1298 cm^{-1} were mainly observed for esters over the TiO_2 (110) surface;[40] bands (1147) cm^{-1} (represents aliphatic esters) and 1032 cm^{-1} (assigned for the aliphatic esters) are also observed. At 150 °C, the bands obtained are similar in the bending region (1799, 1750, 1712, 1674, 1588, 1548, 1510, 1480, 1295, 1150, 1129, and 1039) cm^{-1} [Figure 12B(e)] with the difference in intensity of these bands. The bands at (1799, 1674, 1548, 1510, 1495, and 1293) cm^{-1} systematically increase in intensity as a function of temperature. In the stretch part also, the intensity of the negative bands increases. At higher temperatures like (250 and 300) °C, the intermediates are the same. However, there is one noticeable thing that the peaks (2364 and 2332) cm^{-1} representing the C═O stretching vibrations of gas phase CO_2 molecules also increase as a function of temperature (Figure 12A). This intensity, though much lower than the reaction effect with air, still is more as compared to that of the $BaWO_4$ catalyst. Therefore, with He, the toluene is adsorbed as a π-ring complex, and the lattice oxygen leads to oxidation of it to benzaldehyde, benzoate, aliphatic aldehyde, aliphatic acetate/carboxylate, aliphatic ester, and finally to CO_2. The result of the reaction with toluene and He over the $BaMo_{0.5}W_{0.5}O_4$ catalyst surface is summarized in Scheme 9.

3.5. X-ray Photoelectron Spectroscopy Studies. The XPS studies were carried out on these catalytic samples initially to understand the effect of doping W in the $BaMoO_4$ lattice or vice versa. The other more important objective was to understand the effective active sites that are responsible for the process of adsorption and thermal catalytic reaction of toluene and air, resulting in the formation of surface intermediates that are described in the above section in the different schemes.

The binding energy obtained from the XPS spectra of Ba-3d of the $BaMoO_4$ system, as shown in Figure S1, is obtained at 779.3 and 794.6 eV, respectively, for $3d_{5/2}$ and $3d_{3/2}$ orbitals with l-s splitting parameter ($\Delta\varepsilon$ = 15.3 eV), which is consistent with the earlier literature.[71] The respective binding energy for Ba-3d for the $BaWO_4$ system is at (779.2 and 794.5) eV, which is also consistent with earlier reported data.[72] However, there is no change in the binding energy of the Ba-3d peaks for the $BaMo_{0.5}W_{0.5}O_4$ system (779.3 and 794.6 eV), as has been observed for other $BaCaWO_4$ systems. This signifies that the doping of Mo^{6+} in the W^{6+} lattice does not alter the electron density around Ba^{3+}. The binding energy for O-1s for XPS (Figure S3) peaks for $BaMoO_4$ is obtained at 529.6 eV representing the O-present in the $BaMoO_4$ lattice and at 531.2 eV representing the surface −OH groups of the $BaMoO_4$ catalytic surface. Similarly, XPS data showing binding energy of Mo-3d and W-4f (Figure S2) show Mo-$3d_{5/2}$ and Mo-$3d_{3/2}$ and $BaMoO_4$ and $BaMo_{0.5}W_{0.5}O_4$ to be the same {(231.8 and 234.9) eV and W $4f_{7/2}$ and $4f_{5/2}$ [(34.7 and 36.8) eV: $BaWO_4$ and (35.0 and 37.2) eV: $BaMo_{0.5}W_{0.5}O_4$]}. This mostly shows the fact that the electronic environment in the lattice is unaltered by the doping of Mo in the $BaWO_4$ lattice, mostly due to the fact that the ionic radii of both Mo^{6+} and W^{6+} are almost equal. Binding energy for O-1s XPS spectra (Figure S3) for $BaWO_4$ is obtained at (529.8 and 530.1) eV, where the primary peak corresponds to lattice O of the $BaWO_4$ and the second one surface −OH group.

Figure 12 shows the XPS spectra for the $BaMoO_4$ catalyst both before and after the thermal oxidation of toluene and air. As shown earlier, the binding energy for corresponding Ba-$3d_{5/2}$ and $3d_{3/2}$ is found at (779.6 and 794.6) eV, as was observed in $BaMoO_4$. However, post reaction, the binding energy of the Ba-3d is lowered by 1.3 eV (778.3 and 793.3) eV, which definitely suggests a slight reduction, or increment in the electron density around the Ba^{2+} site. This is mostly because during the reaction, Ba^{2+} has accepted some of the electron or

https://doi.org/10.1021/acsomega.4c10501
ACS Omega 2025, 10, 13080−13104

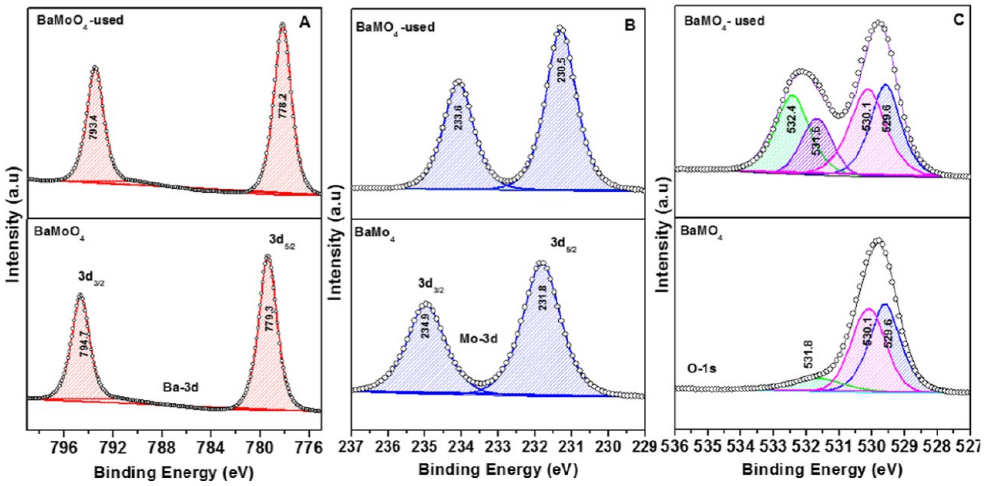

Figure 13. Comparison of the XPS data for the catalysts used before and after catalytic experiments $BaMoO_4$: (A) Ba-3d; (B) Mo-3d; and (C) O-1s.

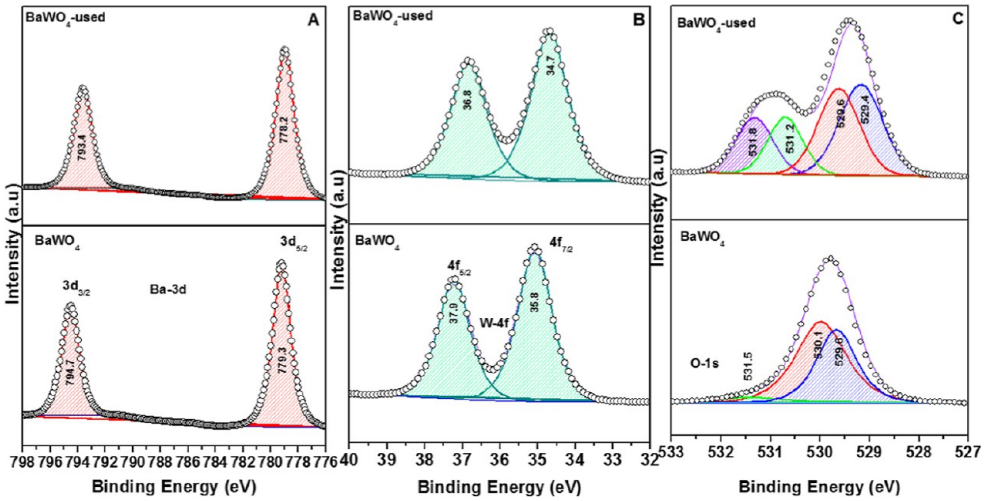

Figure 14. Comparison of the XPS data for the catalysts used before and after catalytic experiments $BaWO_4$: (A) W-4f; (B) Ba-3d; and (C) O-1s.

increment in the electron density around the Ba^{2+} site. This is mostly because during the reaction, Ba^{2+} has accepted some of the electron that has been released in the oxidation of the intermediates over the $BaMoO_4$ surface and thereby is direct evidence of the fact that Ba is one of the active sites where adsorption/reaction occurs over the $BaMoO_4$ surface. While observing the Mo −3d XPS spectra, there is a significant lowering in binding energy of 2.2 eV. The binding energy corresponding to the used sample is at 229.6 and 232.7 eV for Mo $3d_{5/2}$ and $3d_{3/2}$, respectively. This demonstrates that there is a definite increase in the electron density around Mo^{6+} in $BaMoO_4$. Consistent with the previous literature, these binding energies corroborate with the Mo^{5+} state.[73,74] Therefore, Mo^{6+} is the main active site that promotes adsorption and gains the electron to promote the oxidative intermediates over its surface, as shown in the previous schemes. The XPS spectrum for O-1s (Figure 13C) is also very interesting for the used samples. Along with the lattice oxygen for $BaMoO_4$ (O-529.8 eV) and the −O (−OH− 531.2 eV), there is a definite peak at 532.3 eV, which correlates to that of the O-vacancy, and the intensity of this peak is quite high. In the used $BaMoO_4$ lattice, there is presence of Mo as Mo^{5+} and Ba also in a lower oxidation state; therefore, to maintain the lattice charge, some O-vacancy is expected. However, the O-vacancy will not be to this extent as we observe here; therefore, it signifies that certain surface lattice O- is also involved in the oxidation reaction, which is amply proven by the reaction in the He atmosphere.

Figure 14 shows the XPS data for the $BaWO_4$ catalytic surface before and after the catalytic reactions were performed. The alteration in the binding energy for Ba in the $BaWO_4$ catalyst is around 1.2 eV (778.0 eV from 779.2 eV) for the used $BaWO_4$ catalyst. Therefore, over the $BaWO_4$ catalyst also, Ba is also an active site as in the case of $BaMoO_4$ catalyst and the electron density around Ba^{2+} is increased considerably so that it is able to promote the oxidative intermediates. Once we check the W^{6+} (Figure 14A) post, the used $BaWO_4$ catalyst is around 0.5 eV, which shows that W^{6+} is not reduced to the extent of W^{5+} as observed in the layered pyrochlore $Bi_2W_2O_7$.[75] However, the most fascinating part is that of the O-1s in the $BaWO_4$ (Figure 14C) after the catalytic reaction. It shows the (Table for O-1s) three peaks at 530.1, 531.6, and 532.3 eV, respectively. The first O- peak is for the lattice of the $BaWO_4$, which is 0.3 eV higher as compared to the lattice of the $BaWO_4$ unused catalyst (529.8 eV). This alteration in the binding energy is mostly due to the fact that over the $BaWO_4$ catalytic surface, there are several bound intermediates to the O- of the

https://doi.org/10.1021/acsomega.4c10501
ACS Omega 2025, 10, 13080−13104

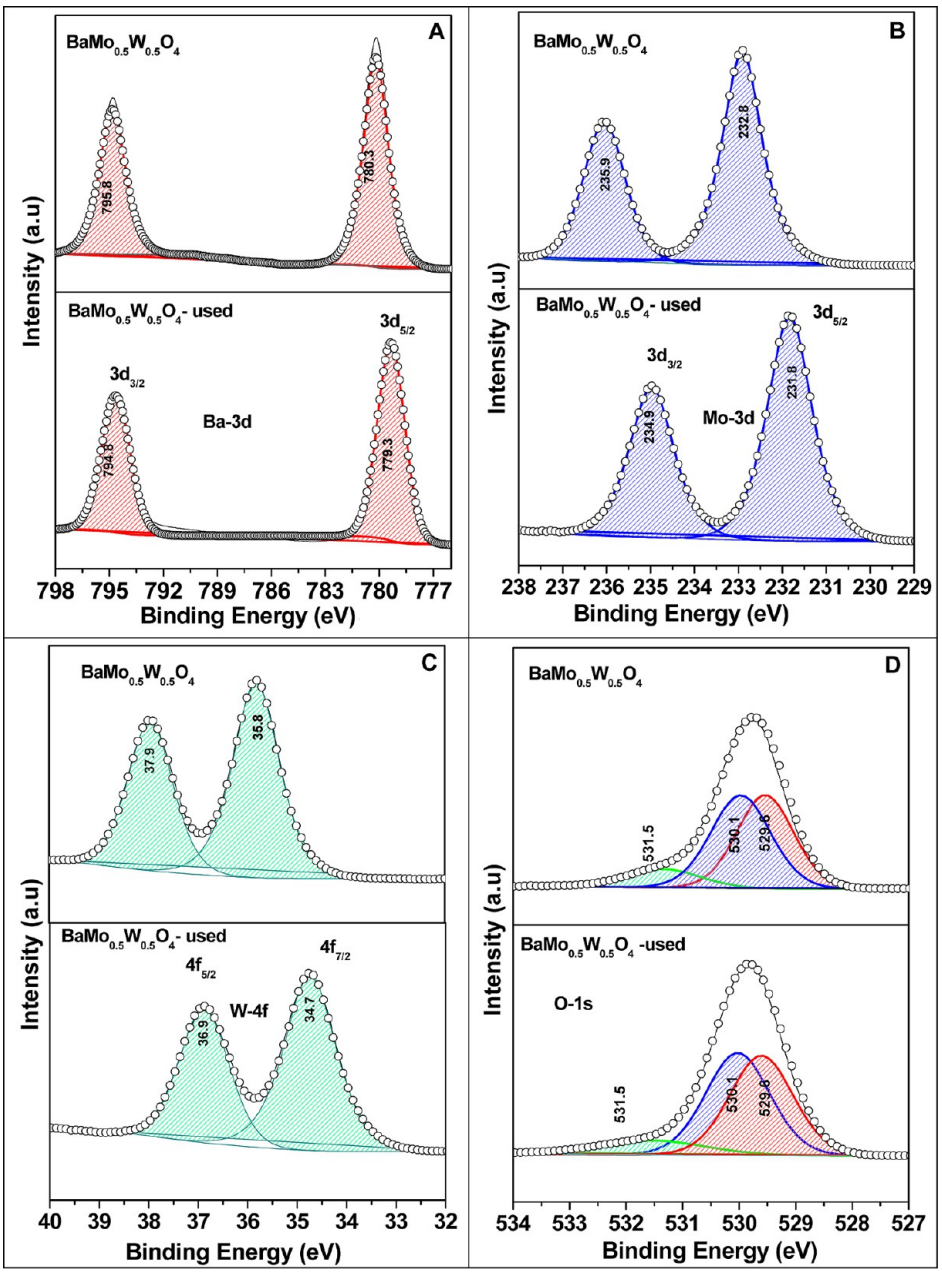

Figure 15. Comparison of the XPS data for the catalysts used before and after catalytic experiments of $BaMo_{0.5}W_{0.5}O_4$: (A) Mo-3d; (B) W-4f; (C) Ba-3d; and (D) O-1s.

lattice, which probably lowers the electron density around O, thereby increasing the B.E of the lattice O-1s, which was not observed over the $BaMoO_4$ catalyst. The -surface −OH group (531.6 eV) for the used catalyst is much less as compared to that of the native $BaWO_4$ catalysts, thereby showing the use of them as suggested in the in situ FT-IR intermediates. The nest peak at 532.3 eV either represents the O-vacancy, which is caused by the use of the lattice O- to oxidize the intermediates even during adsorption (Scheme 4), or represents the O -for the C═O moieties present over the surface.

Mostly going by the intensity of this peak, it is a mixture of these two types. Therefore, the XPS study summarizes that over the $BaWO_4$ surface, the effective active sites are along with Ba and W surface lattice O.

The XPS spectra for the $BaMo_{0.5}W_{0.5}O_4$ catalyst both before and after the thermal oxidation of toluene and air are shown in Figure 15. In Figure 15A, Mo-3d shows lowering of the binding energy of the catalyst after use by 1.1 eV (Mo-$3d_{5/2}$-232.9 eV and after usage Mo-$3d_{5/2}$-231.8 eV). This lowering in binding energy for Ba^{2+} ($BaMo_{0.5}W_{0.5}O_4$ used catalyst) shows increase in the electron density around Ba^{2+} resulting almost in reduction of Ba^{2+} and is similar to that of the $BaMoO_4$ and $BaWO_4$ system. The W-4f system (Figure 15.B) shows lowering in the binding energy of the used sample of 1.1 eV ($4f_{7/2}$-35.8 eV and used one $4f_{7/2}$—34.7 eV), which is much greater as compared to the $BaWO_4$ system.

Therefore, in the $BaMo_{0.5}W_{0.5}O_4$ used catalyst, the W is reduced to the extent of W^{5+} consistent with the earlier literature.[76,77] The Mo-3d-XPS of the used $BaMo_{0.5}W_{0.5}O_4$ catalyst (Figure 15.C) shows a lowering in the binding energy also by 1.1 eV ($3d_{5/2}$—780.4 eV and used $3d_{5/2}$—779.3 eV) much lower as compared to that in $BaMoO_4$ catalytic surface,

https://doi.org/10.1021/acsomega.4c10501
ACS Omega 2025, 10, 13080−13104

Scheme 10. Representation of the Surface Process from XPS[a]

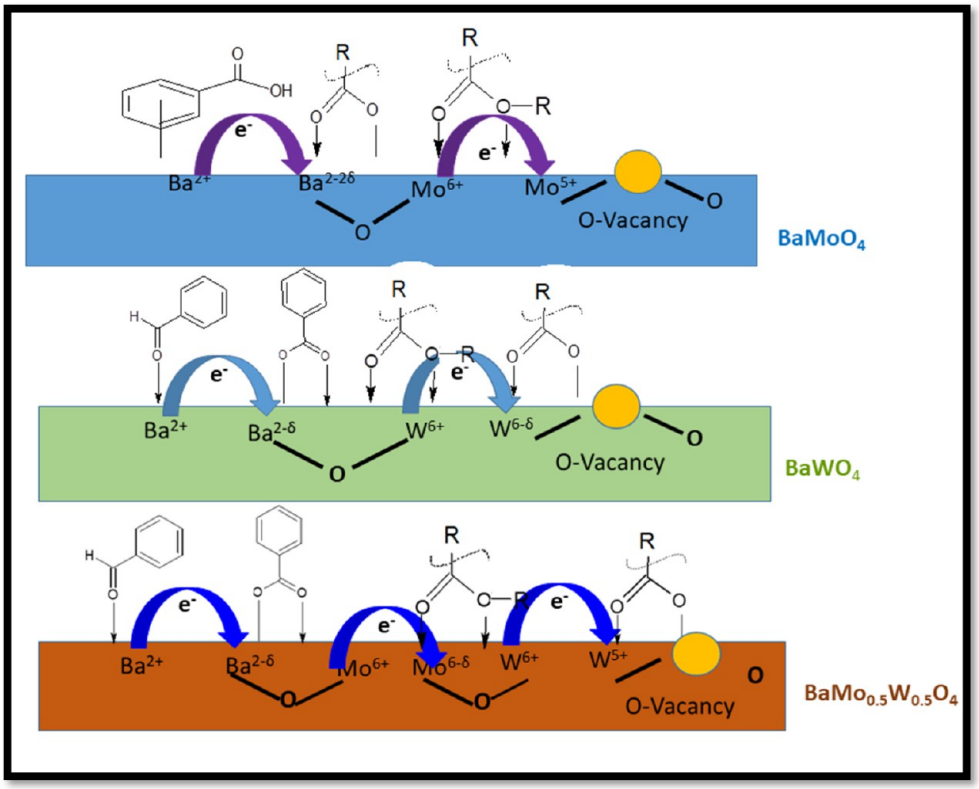

[a]This is a mere representation and has got nothing to do with actual structures.

which shows that reduction of the Mo site of the $BaMo_{0.5}W_{0.5}O_4$ used catalyst is much lower as compared to that of $BaMoO_4$. This is an indication that the W^{6+} site is most probably more utilized in the $BaMo_{0.5}W_{0.5}O_4$ catalyst as compared to that of the Mo^{6+} site.

This understanding is also understood from the in situ FT-IR intermediates, where intermediates formed over the $BaMo_{0.5}W_{0.5}O_4$ catalyst are more similar with the $BaWO_4$ catalytic set, as compared to the $BaMoO_4$ catalytic set. The O-1s XPS spectra (Figure 15D) shown in the used $BaMo_{0.5}W_{0.5}O_4$ catalyst, there is no shift for the O- corresponding to the lattice −O. The latter peak of O (unused sample) corresponds to -surface −OH (530.8) eV and has a positive shift in the binding energy (531.4 eV). This positive shift (∼1 eV) mostly indicates O-vacancies or that of the O corresponding to the O═C from the surface intermediates. With the intensity of this peak much lower as compared to that of the $BaWO_4/BaMoO_4$ catalyst and with the reduction in the W^{6+} charge center (absent for $BaWO_4$), it can be speculated as the O-vacancy peaks. The XPS understanding is summarized in Scheme 10.

3.6. Discussion. The different intermediates that are formed over the surface of the different catalysts are as follows: $BaMoO_4$ adsorbs toluene with the π-ring of the benzene and upon reaction produces aldehydic species, acetate ester, and finally CO_2. $BaWO_4$, on the other hand, adsorbs toluene by reactive adsorption, forming benzaldehyde and benzoate. Upon thermal reaction, the different intermediates formed are aldehyde, carboxylate/acetates, esters, and finally CO_2. $BaMo_{0.5}W_{0.5}O_4$ also forms reactive adsorption, forming benzaldehyde and benzoates as adsorbed intermediates. Upon reaction, the reactive intermediates formed are aldehydes, acetates ester, and CO_2 from the adsorbed benzoates. The XPS studies show that the surface electron density of all the catalysts is increased around the Ba^{2+} site forming $Ba^{2-\delta}$ and in the $BaMoO_4$ catalyst in the Mo-site Mo^{6+} forms Mo^{5+} after adsorption/reaction, which acts as a hard base (gains electron density in the process of oxidation of the intermediates) and would thereby stabilize a stronger nucleophile like carboxylate as intermediates. However, in $BaWO_4$, W^{6+} goes to $W^{6-\delta}$ after adsorption, which will be a soft base, thereby stabilizing the weaker nucleophiles like esters and acetates as oxidizes finally to CO_2. However, in $BaMo_{0.5}W_{0.5}O_4$, there are two states (a) Mo site, where Mo^{6+}shifts to $Mo^{6-\delta}$ being a weaker basic site, and (b) W-site, where W^{6+} goes to W^{5+} after reaction showing a harder basic site. Therefore, $BaMo_{0.5}W_{0.5}O_4$ will have both the harder and the softer basic sites and will be able to stabilize both stronger and weaker nucleophiles like carboxylates and acetates and esters together. Also, in the $BaMo_{0.5}W_{0.5}O_4$, two different sites mostly in the two different planes for adsorption of Mo^{6+} and W^{6+} will definitely cause a considerable ring strain, making the reaction kinetics faster as is observed. Therefore, the presence of both the hard and softer basic sites as well as the ring strain caused by two different adsorption sites makes the $BaMo_{0.5}W_{0.5}O_4$, a better thermal catalyst. Similarly, the O-vacancies will be more strongly effective in $BaMo_{0.5}W_{0.5}O_4$ owing to its differential electron density in Mo and W, further facilitating the reaction.

There are certain questions that should be taken here. (a) How does the surface of the $BaMoO_4$ and $BaWO_4$ despite having almost similar surface characteristics lead to the formation of different intermediates even during adsorption? (b) How under a nonoxidative condition toluene is oxidized to form CO_2 in the case of $BaWO_4$ and $BaMo_{0.5}W_{0.5}O_4$? (c) Why

https://doi.org/10.1021/acsomega.4c10501
ACS Omega 2025, 10, 13080−13104

does in the $BaMo_{0.5}W_{0.5}O_4$ the intermediates of the $BaWO_4$ catalytic surface takes precedence in comparison to $BaMoO_4$? (d) How does the Scheelite completely mineralize toluene and air? The Scheelite $BaMoO_4$ and $BaWO_4$ possess Mo^{6+} and W^{6+} with similar ionic radii, yet the W^{6+} possesses f-orbitals, which can accommodate more electrons as compared to that of Mo^{6+}, and mostly, the adsorption of $BaWO_4$ and $BaMoO_4$ occurs at different surfaces with different surface energies. The benzaldehyde and benzoate formation during the adsorption process probably is due to lower interaction energy or stabilization energy, which at this moment is still an open question and is tough to understand from the present set of data presented by the different intermediates formed. The second question prompts the answer that the lattice oxygen is definitely involved in the oxidation process, which becomes very clear during the toluene oxidation process in He medium. In the absence of oxygen, astonishingly, all the catalysts degrade *toluene* completely to the extent of CO_2, thereby showing a definite Mars and Van Krevelen (MVK) type of mechanism. Also, the major question is that of the energetics of the surface and the stability of these intermediates, as shown in the different schemes over the different active sites over $BaMo_{0.5}W_{0.5}O_4$. From XPS, it is quite clear that in $BaMo_{0.5}W_{0.5}O_4$, the W site is a far and more active site as compared to that of Ba^{2+}/Mo^{6+}/O-vacancies. Therefore, it is quite regulatory that the $BaMo_{0.5}W_{0.5}O_4$ catalytic surface generically behaves with W-oriented intermediates, as compared to that of the Mo-oriented ones. However, studies on the energetics of the different intermediates over these surfaces are out of the scope of this article and shall be undertaken separately in support of this conclusion.

4. CONCLUSIONS

The complete mineralization of toluene (a very stable organic molecule) in the presence and absence of air has been studied with the Scheelite catalysts: $BaMo_{0.5}W_{0.5}O_4$, $BaWO_4$, and $BaMO_4$. The $BaMo_{0.5}W_{0.5}O_4$ catalyst shows one of the lowest mineralization temperatures (~200 °C) among all the oxide thermal catalysts reported so far for toluene mineralization. The rate of toluene mineralization using these catalysts is in the order $BaMo_{0.5}W_{0.5}O_4 \gg BaWO_4 > BaMO_4$. The in situ FT-IR studies as a function of temperature in the presence of air show different intermediates over $BaMoO_4$ as: aldehyde, acetates, and ester. Similarly, over $BaWO_4$, the different intermediates formed are benzaldehyde, benzoates, aldehydes, carboxylates, and ester. The $BaMo_{0.5}W_{0.5}O_4$ catalysts show benzaldehyde, benzoates, aldehydes, acetates, and ester as different intermediates. The final product obtained for toluene degradation for all three catalysts is CO_2. The different intermediates formed over these Scheelite catalysts in the absence of oxygen have also been understood thoroughly, showing the effect of lattice oxygen to produce CO_2. The XPS studies show that for the $BaMoO_4$ catalysts, a certain amount of electron density is increased, from the Ba^{2+} site forming $Ba^{2-\delta}$; similarly, for Mo site, Mo^{6+} produces Mo^{5+} after adsorption/reaction. This acts as a hard base stabilizing stronger nucleophile like carboxylates as intermediates. However, in $BaWO_4$, the W^{6+} goes to $W^{6-\delta}$ post adsorption/reaction acting as a softer base, thereby stabilizing the weaker nucleophiles like esters and acetates. However, in $BaMo_{0.5}W_{0.5}O_4$, two states are present: (a) Mo site—Mo^{6+} forms $Mo^{6-\delta}$, acting as a softer base; and (b) W site, where W^{6+} goes to W^{5+}, acting as a harder base in the process of adsorption/reaction. This will lead to the stabilization of both stronger and weaker nucleophiles together. $BaMo_{0.5}W_{0.5}O_4$ also causes ring strain due to the presence of two different Mo^{6+} and W^{6+} at different planes. These factors make $BaMo_{0.5}W_{0.5}O_4$ a better thermal catalyst as compared to the other catalysts ($BaWO_4$ and $BaMoO_4$). These active sites for these catalysts in the absence of oxygen show a definite Mars and Van Krevelen (MVK) type of mechanism, where the labile lattice oxygen also plays a strong role in the catalytic efficiency. These catalysts will hopefully pave new pathways for the toluene degradation using mixed oxide catalysts in industrial scale.

ASSOCIATED CONTENT

Supporting Information

The Supporting Information is available free of charge at https://pubs.acs.org/doi/10.1021/acsomega.4c10501.

Ba-3d XPS data for different samples, XPS data for Mo-3d for the different samples, XPS data for O-1s for the different samples, adsorption and reaction of toluene and air over the $BaMoO_4$ catalyst as a function of time at 200 °C, adsorption and reaction of toluene and air over the $BaWO_4$ catalyst as a function of time at 200 °C, adsorption and reaction of toluene and air over the $BaMo_{0.5}W_{0.5}O_4$ catalyst as a function of time at 150 °C, indexing for SAED, SEM image for $BaWO_4$ along with the elemental mapping and the EDS spectra for the $BaWO_4$, and SEM image for $BaMoO_4$ along with the elemental mapping and the EDS spectra for the $BaMoO_4$ (PDF)

AUTHOR INFORMATION

Corresponding Author

Kaustava Bhattacharyya − *Chemistry Division, Bhabha Atomic Research Centre, Mumbai 400 085, India; Homi Bhabha National Institute, Mumbai 400 094, India;* orcid.org/0000-0003-4901-2814; Email: kaustava@barc.gov.in

Authors

Mohsin Jafar − *Chemistry Division, Bhabha Atomic Research Centre, Mumbai 400 085, India*

Adarsh Kumar − *Chemistry Division, Bhabha Atomic Research Centre, Mumbai 400 085, India; Homi Bhabha National Institute, Mumbai 400 094, India*

Vinita G. Gupta − *Chemistry Division, Bhabha Atomic Research Centre, Mumbai 400 085, India; Homi Bhabha National Institute, Mumbai 400 094, India;* orcid.org/0000-0001-9139-2369

Avesh K. Tyagi − *Homi Bhabha National Institute, Mumbai 400 094, India;* orcid.org/0000-0002-4268-1364

Complete contact information is available at: https://pubs.acs.org/10.1021/acsomega.4c10501

Author Contributions

[§]M.J. and A.K. contributed equally to this work.

Notes

The authors declare no competing financial interest.

ACKNOWLEDGMENTS

Dr. Naveen Kumar and Dr. V. Biswanadh of Material Science Division, BARC, for the HR-TEM experiments, Dr. Venkat

Krishnan, IIT Mandi, for his help in taking XPS data, and Shri Aseesh Kumar of BARC, ChD, for taking SEM and elemental mapping and EDS data. There were no financial grants involved for the work related to this manuscript.

REFERENCES

(1) Cheng, Q.; Li, Y.; Wang, Z.; Wang, X.; Zhang, G. Boosting full-spectrum light driven surface lattice oxygen activation of $ZnMn_2O_4$ by facet engineering for highly efficient photothermal mineralization of toluene. *Appl. Catal. B Environ.* **2023**, *324*, 122274.
(2) Zhang, J.; Hu, Y.; Qin, J.; Yang, Z.; Fu, M. TiO_2-UiO-66-NH_2 nanocomposites as efficient photocatalysts for the oxidation of VOCs. *Chem. Eng. J.* **2020**, *385*, 123814.
(3) Shayegan, Z.; Lee, C.-S.; Haghighat, F. TiO_2 photocatalyst for removal of volatile organic compounds in gas phase−A review. *Chem. Eng. J.* **2018**, *334*, 2408−2439.
(4) Zhong, L.; Brancho, J. J.; Batterman, S.; Bartlett, B. M.; Godwin, C. Experimental and modeling study of visible light responsive photocatalytic oxidation (PCO) materials for toluene degradation. *Appl. Catal. B Environ.* **2017**, *216*, 122−132.
(5) Zhu, T.; Li, J.; Liang, W.; Jin, Y. Synergistic effect of catalyst for oxidation removal of toluene. *J. Hazard Mater.* **2009**, *165* (1−3), 1258−1260.
(6) Zhu, T.; Li, J.; Jin, Y. Q.; Liang, Y. H.; Ma, G. D. Gaseous phase benzene decomposition by non-thermal plasma coupled with nano titania catalyst. *Int. J. Environ. Sci. Technol.* **2009**, *6*, 141−148.
(7) Liang, W.-J.; Ma, L.; Liu, H.; Li, J. Toluene degradation by non-thermal plasma combined with a ferroelectric catalyst. *Chemosphere* **2013**, *92* (10), 1390−1395.
(8) Wang, Y.; Zhang, Y.; Su, L.; Li, X.; Duan, L.; Wang, C.; Huang, T. Hazardous air pollutant formation from pyrolysis of typical Chinese casting materials. *Environ. Sci. Technol.* **2011**, *45* (15), 6539−6544.
(9) Mok, Y. S.; Nam, C. M.; Cho, M. H.; Nam, I.-S. Decomposition of volatile organic compounds and nitric oxide by nonthermal plasma discharge processes. *IEEE Trans. Plasma Sci.* **2002**, *30* (1), 408−416.
(10) Liang, W. J.; Li, J.; Jin, Y. Q. Photocatalytic degradation of gaseous acetone, toluene, and p-xylene using a TiO_2 thin film. *J. Environ. Sci. Health, Part A* **2010**, *45* (11), 1384−1390.
(11) Peng, R.; Li, S.; Sun, X.; Ren, Q.; Chen, L.; Fu, M.; Wu, J.; Ye, D. Size effect of Pt nanoparticles on the catalytic oxidation of toluene over Pt/CeO_2 catalysts. *Appl. Catal. B Environ.* **2018**, *220*, 462−470.
(12) Xiao, H.; Wu, J.; Wang, X.; Wang, J.; Mo, S.; Fu, M.; Chen, L.; Ye, D. Ozone-enhanced deep catalytic oxidation of toluene over a platinum-ceria-supported BEA zeolite catalyst. *Mol. Catal.* **2018**, *460*, 7−15.
(13) Li, S.; Xu, Y.; Chen, Y.; Li, W.; Lin, L.; Li, M.; Deng, Y.; Wang, X.; Ge, B.; Yang, C.; et al. Tuning the selectivity of catalytic carbon dioxide hydrogenation over iridium/cerium oxide catalysts with a strong metal−support interaction. *Angew. Chem.* **2017**, *129* (36), 10901−10905.
(14) Murata, K.; Mahara, Y.; Ohyama, J.; Yamamoto, Y.; Arai, S.; Satsuma, A. The metal−support interaction concerning the particle size effect of Pd/Al_2O_3 on methane combustion. *Angew. Chem.* **2017**, *129* (50), 16209−16213.
(15) Yan, D.; Li, T.; Liu, P.; Mo, S.; Zhong, J.; Ren, Q.; Sun, Y.; Cheng, H.; Fu, M.; Wu, J.; et al. In-situ atmosphere thermal pyrolysis of spindle-like Ce (OH) CO_3 to fabricate Pt/CeO_2 catalysts: Enhancing Pt−O−Ce bond intensity and boosting toluene degradation. *Chemosphere* **2021**, *279*, 130658.
(16) Yan, D.; Mo, S.; Sun, Y.; Ren, Q.; Feng, Z.; Chen, P.; Wu, J.; Fu, M.; Ye, D. Morphology-activity correlation of electrospun CeO_2 for toluene catalytic combustion. *Chemosphere* **2020**, *247*, 125860.
(17) Wu, K.; Sun, Y.; Liu, J.; Xiong, J.; Wu, J.; Zhang, J.; Fu, M.; Chen, L.; Huang, H.; Ye, D. Nonthermal plasma catalysis for toluene decomposition over $BaTiO_3$-based catalysts by Ce doping at A-sites: The role of surface-reactive oxygen species. *J. Hazard. Mater.* **2021**, *405*, 124156.
(18) Shen, Y.; Liu, S.; Lu, L.; Zhu, C.; Fang, Q.; Liu, R.; He, Z.; Li, Y.; Song, S. Photocatalytic degradation of toluene by a TiO_2 pn homojunction nanostructure. *ACS Appl. Nano Mater.* **2022**, *5* (12), 18612−18621.
(19) Turchi, C. S.; Ollis, D. F. Photocatalytic degradation of organic water contaminants: mechanisms involving hydroxyl radical attack. *J. Catal.* **1990**, *122* (1), 178−192.
(20) Augugliaro, V.; Coluccia, S.; Loddo, V.; Marchese, L.; Martra, G.; Palmisano, L.; Schiavello, M. Photocatalytic oxidation of gaseous toluene on anatase TiO_2 catalyst: mechanistic aspects and FT-IR investigation. *Appl. Catal. B Environ.* **1999**, *20* (1), 15−27.
(21) Ibusuki, T.; Takeuchi, K. Toluene oxidation on UV-irradiated titanium dioxide with and without O_2, NO_2 or H_2O at ambient temperature. *Atmos. Environ.* **1986**, *20* (9), 1711−1715.
(22) Bhattacharyya, K.; Varma, S.; Tripathi, A. K.; Bharadwaj, S. R.; Tyagi, A. K. Mechanistic insight by in situ FTIR for the gas phase photo-oxidation of ethylene by V-doped titania and nano titania. *J. Phys. Chem. B* **2009**, *113* (17), 5917−5928.
(23) Chen, Z.; Peng, Y.; Chen, J.; Wang, C.; Yin, H.; Wang, H.; You, C.; Li, J. Performance and mechanism of photocatalytic toluene degradation and catalyst regeneration by thermal/UV treatment. *Environ. Sci. Technol.* **2020**, *54* (22), 14465−14473.
(24) Lu, Y.; Deng, H.; Pan, T.; Wang, L.; Zhang, C.; He, H. Interaction between noble metals (Pt, Pd, Rh, Ir, Ag) and defect-enriched TiO_2 and its application in toluene and propene catalytic oxidation. *Appl. Surf. Sci.* **2022**, *606*, 154834.
(25) Yin, X.; Shen, L.; Wang, S.; Wang, B.; Shen, C. Double adjustment of Co and Sr in $LaMnO_3^{+\delta}$ perovskite oxygen carriers for chemical looping steam methane reforming. *Appl. Catal. B Environ.* **2022**, *301*, 120816.
(26) Cao, R.; Li, L.; Zhang, P.; Gao, L.; Rong, S. Regulating oxygen vacancies in ultrathin δ-MnO_2 nanosheets with superior activity for gaseous ozone decomposition. *Environ. Sci.: Nano* **2021**, *8* (6), 1628−1641.
(27) Alencar, L. D. d. S.; Lima, N. A.; Mesquita, A.; Probst, L. F. D.; Batalha, D. C.; Rosmaninho, M. G.; Fajardo, H. V.; Balzer, R.; Bernardi, M. I. B. Effect of different synthesis methods on the textural properties of calcium tungstate ($CaWO_4$) and its catalytic properties in the toluene oxidation. *Mater. Res.* **2018**, *21* (3), No. e20170961.
(28) Berenjian, A.; Fathi, A.; Feghenabi, S.; Khodiev, A. Complete removal of toluene from air: a response surface methodology. *Aust. J. Basic Appl. Sci.* **2011**, *5* (6), 286−288.
(29) Muñoz, R.; Villaverde, S.; Guieysse, B.; Revah, S. Two-phase partitioning bioreactors for treatment of volatile organic compounds. *Biotechnol. Adv.* **2007**, *25* (4), 410−422.
(30) Khan, F. I.; Kr Ghoshal, A. Removal of volatile organic compounds from polluted air. *J. Loss Prev. Process. Ind.* **2000**, *13* (6), 527−545.
(31) Li, J.; Li, Y.; Wang, X.; Yang, Z.; Zhang, G. Atomically dispersed Fe sites on TiO_2 for boosting photocatalytic CO_2 reduction: Enhanced catalytic activity, DFT calculations and mechanistic insight. *Chin. J. Catal.* **2023**, *51*, 145−156.
(32) Yue, W.; Lei, W.; Dong, Y.; Shi, C.; Lu, Q.; Cui, X.; Wang, X.; Chen, Y.; Zhang, J. Toluene degradation in air/H_2O DBD plasma: A reaction mechanism investigation based on detailed kinetic modeling and emission spectrum analysis. *J. Hazard. Mater.* **2023**, *448*, 130894.
(33) Gopinath, M.; Dhanasekar, R. Microbial degradation of toluene. *Afr. J. Biotechnol.* **2012**, *11* (96), 16210−16219.
(34) Xu, Z.; Mo, S.; Li, Y.; Zhang, Y.; Wu, J.; Fu, M.; Niu, X.; Hu, Y.; Ye, D. Pt/MnOx for toluene mineralization via ozonation catalysis at low temperature: SMSI optimization of surface oxygen species. *Chemosphere* **2022**, *286*, 131754.
(35) Panchal, V.; Garg, N.; Sharma, S. M. Raman and x-ray diffraction investigations on $BaMoO_4$ under high pressures. *J. Phys.: Condens. Matter* **2006**, *18* (16), 3917.
(36) Khor, A.; Leung, P.; Mohamed, M. R.; Flox, C.; Xu, Q.; An, L.; Wills, R. G. A.; Morante, J. R.; Shah, A. A. Review of zinc-based hybrid flow batteries: From fundamentals to applications. *Mater. Today Energy* **2018**, *8*, 80−e108.

https://doi.org/10.1021/acsomega.4c10501
ACS Omega 2025, 10, 13080−13104

(37) Li, X.; Wang, Y.; He, J.; Xiao, J.; Xu, W.; Chen, D.; Li, N.; Xu, Q.; Li, H.; Lu, J. Combination of porous covalent triazine frameworks with spinel for highly improved photothermal catalytic oxidation of toluene. *Appl. Catal. B Environ.* **2023**, *331*, 122690.
(38) Bodziony, T.; Kaczmarek, S. M. Structural Analysis of the $BaWO_4$ Crystal Doped with Ce and Codoped with Na Ions Based on g-shift Parameters. *Crystals* **2020**, *10* (9), 789.
(39) Zhang, Y. In-situ IR study for elucidating the adsorption cracking mechanism of toluene over calcined olivine catalyst. *Int. J. Hydrogen Energy* **2018**, *43* (33), 15835−15842.
(40) Yuan, J.; Li, G.; Liu, X.; Yang, Y.; Yu, F.; Cao, J.; Fei, Z.; Ma, J.; Nazeeruddin, M. K.; Dyson, P. J. Catalytic Oxidation of BTX (Benzene, Toluene, and Xylene) Using Metal Oxide Perovskites. *Adv. Funct. Mater.* **2024**, *34*, 2401281.
(41) Boonruam, P.; Neramittagapong, S.; Neramittagapong, A.; Wantala, K. Toluene Degradation by Thermal Catalytic Oxidation over K-OMS-2 Catalysts. *Adv. Mater. Res.* **2014**, *931*−*932*, 22−26.
(42) Yao, S.; Chen, Z.; Xie, H.; Yuan, Y.; Zhou, R.; Xu, B.; Chen, J.; Wu, X.; Wu, Z.; Jiang, B.; Tang, X.; Lu, H.; Nozaki, T.; Kim, H.-H. Highly efficient decomposition of toluene using a high-temperature plasma-catalysis reactor. *Chemosphere* **2020**, *247*, 125863.
(43) Bai, Y.; Yang, X.; Chen, J.; Shen, B. The removal of toluene by thermoscatalytic oxidation using CeO_2-based catalysts:a review. *Chemosphere* **2024**, *351*, 141253.
(44) Bi, F.; Feng, X.; Zhou, Z.; Zhang, Y.; Wei, J.; Yuan, L.; Liu, B.; Huang, Y.; Zhang, X. Mn-based catalysts derived from the non-thermal treatment of Mn-MIL-100 to enhance its water-resistance for toluene oxidation: Mechanism study. *Chem. Eng. J.* **2024**, *485*, 149776.
(45) Yuan, J.; Li, G.; Liu, X.; Yang, Y.; Yu, F.; Cao, J.; Fei, Z.; Ma, J.; Nazeeruddin, M. K.; Dyson, P. J. Catalytic Oxidation of BTX (Benzene, Toluene, and Xylene) Using Metal Oxide Perovskites. *Adv. Funct. Mater.* **2024**, *34*, 2401281.
(46) Mukai, D.; Murai, Y.; Higo, T.; Tochiya, S.; Hashimoto, T.; Sugiura, Y.; Sekine, Y. In situ IR study for elucidating reaction mechanism of toluene steam reforming over $Ni/La_{0.7}Sr_{0.3}AlO_{3-\delta}$ catalyst. *Appl. Catal., A* **2013**, *466*, 190−197.
(47) Yang, C. C.; Chang, S. H.; Hong, B. Z.; Chi, K. H.; Chang, M. B. Innovative PCDD/F-containing gas stream generating system applied in catalytic decomposition of gaseous dioxins over V_2O_5−WO_3/TiO_2-based catalysts. *Chemosphere* **2008**, *73* (6), 890−895.
(48) Van den Brink, R. W.; Krzan, M.; Feijen-Jeurissen, M. M. R.; Louw, R.; Mulder, P. The role of the support and dispersion in the catalytic combustion of chlorobenzene on noble metal based catalysts. *Appl. Catal. B Environ.* **2000**, *24* (3−4), 255−264.
(49) Joseph, T.; Halligudi, S. B.; Satyanarayan, C.; Sawant, D. P.; Gopinathan, S. Oxidation by molecular oxygen using zeolite encapsulated Co(II)saloph complexes. *J. Mol. Catal. A: Chem.* **2001**, *168* (1), 87−97.
(50) Hernández-Alonso, M. D.; Tejedor-Tejedor, I.; Coronado, J. M.; Anderson, M. A. Operando FTIR study of the photocatalytic oxidation of methylcyclohexane and toluene in air over TiO_2−ZrO_2 thin films: Influence of the aromaticity of the target molecule on deactivation. *Appl. Catal. B Environ.* **2011**, *101* (3−4), 283−293.
(51) Sun, J.; Li, X.; Zhao, Q.; Ke, J.; Zhang, D. Novel $V_2O_5/BiVO_4/TiO_2$ nanocomposites with high visible-light-induced photocatalytic activity for the degradation of toluene. *J. Phys. Chem. C* **2014**, *118* (19), 10113−10121.
(52) Shao, J.; Lin, F.; Wang, Z.; Liu, P.; Tang, H.; He, Y.; Cen, K. Low temperature catalytic ozonation of toluene in flue gas over Mn-based catalysts: Effect of support property and SO_2/water vapor addition. *Appl. Catal. B Environ.* **2020**, *266*, 118662.
(53) Lin, H.; Long, J.; Gu, Q.; Zhang, W.; Ruan, R.; Li, Z.; Wang, X. In situ IR study of surface hydroxyl species of dehydrated TiO_2: towards understanding pivotal surface processes of TiO_2 photo-catalytic oxidation of toluene. *Phys. Chem. Chem. Phys.* **2012**, *14* (26), 9468−9474.
(54) Buchholz, M.; Xu, M.; Noei, H.; Weidler, P.; Nefedov, A.; Fink, K.; Wang, Y.; Wöll, C. Interaction of carboxylic acids with rutile TiO_2 (110): IR-investigations of terephthalic and benzoic acid adsorbed on a single crystal substrate. *Surf. Sci.* **2016**, *643*, 117−123.
(55) Smith, B. C. *Infrared Spectral Interpretation: A Systematic Approach*; CRC Press, 2018.
(56) Kumar, A.; Tyagi, D.; Varma, S.; Chand, H.; Krishnan, V.; Bhattacharyya, K.; Tyagi, A. K. Thermal catalytic mineralization of ortho-dichlorobenzene at low temperature: an in situ FT-IR and XPS mechanistic investigation. *Mater. Adv.* **2024**, *5* (3), 1301−1331.
(57) Bhattacharyya, K.; Kumar, A.; Tyagi, D.; Tripathi, A. K.; Tyagi, A. K. Role of Constituent Oxides for Thermal Mineralization of o-Dichloro Benzene over Mixed-Oxide-TiO_2 Catalysts: A Mechanistic Explanation. *ChemPhysChem* **2024**, *25* (11), No. e202300472.
(58) Karthick, N. K.; Arivazhagan, G.; Shanmugam, R. FTIR spectroscopic studies and DFT calculations on the toluene-propionitrile binary system. *J. Mol. Struct.* **2018**, *1173*, 456−461.
(59) Sun, J.; Li, X.; Zhao, Q.; Tadé, M. O.; Liu, S. Quantum-sized $BiVO_4$ modified TiO_2 microflower composite heterostructures: efficient production of hydroxyl radicals towards visible light-driven degradation of gaseous toluene. *J. Mater. Chem. A* **2015**, *3* (43), 21655−21663.
(60) Blount, M. C.; Falconer, J. L. Characterization of Adsorbed Species on TiO_2 after Photocatalytic Oxidation of Toluene. *J. Catal.* **2001**, *200* (1), 21−33.
(61) Besselmann, S.; Löffler, E.; Muhler, M. On the role of monomeric vanadyl species in toluene adsorption and oxidation on V_2O_5/TiO_2 catalysts: a Raman and in situ DRIFTS study. *J. Mol. Catal. A: Chem.* **2000**, *162* (1−2), 401−411.
(62) Busca, G.; Cavani, F.; Trifirò, F. Oxidation and ammoxidation of toluene over vanadium-titanium oxide catalysts: a Fourier transform infrared and flow reactor study. *J. Catal.* **1987**, *106* (2), 471−482.
(63) Wachs, I. E.; Weckhuysen, B. M. Structure and reactivity of surface vanadium oxide species on oxide supports. *Appl. Catal., A* **1997**, *157* (1−2), 67−90.
(64) Miyata, H.; Ohno, T.; Hatayama, F. FTIR studies of the interaction of aromatic hydrocarbons with vanadium oxide layered on ZrO_2 and TiO_2. *J. Chem. Soc., Faraday Trans.* **1995**, *91* (19), 3505−3510.
(65) Gan, G.; Yang, Z.; Li, Y.; Zhang, G. Efficient Photothermal Mineralization of Toluene over $MnCo_2O_4$ with Different Exposed Facets: Revealing the Role of Oxygen Vacancy and Photo-/Thermo-Synergistic Mechanism. *Appl. Catal., B* **2024**, *357*, 124308.
(66) Cheng, Q.; Wang, Z.; Wang, X.; Li, J.; Li, Y.; Zhang, G. A novel $Cu_{1.5}Mn_{1.5}O_4$ photothermal catalyst with boosted surface lattice oxygen activation for efficiently photothermal mineralization of toluene. *Nano Res.* **2023**, *16* (2), 2133−2141.
(67) Li, X.; Zhu, Z.; Zhao, Q.; Wang, L. Photocatalytic degradation of gaseous toluene over $ZnAl_2O_4$ prepared by different methods: a comparative study. *J. Hazard. Mater.* **2011**, *186* (2−3), 2089−2096.
(68) Bhattacharyya, K.; Danon, A.; Vijayan, B.; Gray, K. A.; Stair, P. C.; Weitz, E. Role of the surface lewis acid and base sites in the adsorption of CO_2 on titania nanotubes and platinized titania nanotubes: an in situ FT-IR study. *J. Phys. Chem. C* **2013**, *117* (24), 12661−12678.
(69) Liao, L. F.; Lien, C. F.; Shieh, D. L.; Chen, M. T.; Lin, J. L. FTIR study of adsorption and photoassisted oxygen isotopic exchange of carbon monoxide, carbon dioxide, carbonate, and formate on TiO_2. *J. Phys. Chem. B* **2002**, *106* (43), 11240−11245.
(70) Xu, W.; Wang, N.; Chen, Y.; Chen, J.; Xu, X.; Yu, L.; Chen, L.; Wu, J.; Fu, M.; Zhu, A.; et al. In situ FT-IR study and evaluation of toluene abatement in different plasma catalytic systems over metal oxides loaded γ-Al_2O_3. *Catal. Commun.* **2016**, *84*, 61−66.
(71) Emmerling, F.; Reck, G.; Kraus, W.; Orgzall, I.; Schulz, B. Structure determination of two asymmetrically substituted oxadiazoles from powder diffraction data. *Cryst. Res. Technol.* **2008**, *43* (1), 99−107.
(72) Capece, A. M.; Polk, J. E.; Shepherd, J. E. X-ray photoelectron spectroscopy study of $BaWO_4$ and Ba_2CaWO_6. *J. Electron Spectrosc. Relat. Phenom.* **2014**, *197*, 102−105.

https://doi.org/10.1021/acsomega.4c10501
ACS Omega 2025, 10, 13080−13104

(73) Bhattacharyya, K.; Majeed, J.; Dey, K. K.; Ayyub, P.; Tyagi, A. K.; Bharadwaj, S. R. Effect of Mo-Incorporation in the TiO_2 Lattice: A mechanistic basis for photocatalytic dye degradation. *J. Phys. Chem. C* **2014**, *118* (29), 15946−15962.
(74) Cai, X.; Sang, X.-G.; Song, Y.; Guo, D.; Liu, X.-X.; Sun, X. Activating the highly reversible Mo^{4+}/Mo^{5+} redox couple in amorphous molybdenum oxide for high-performance supercapacitors. *ACS Appl. Mater. Interfaces* **2020**, *12* (43), 48565−48571.
(75) Iimura, R.; Hasegawa, T.; Yin, S. Electrochromic behavior originating from the W^{6+}/W^{5+} redox in aurivillius-type tungsten-based layered perovskites. *Inorg. Chem.* **2022**, *61* (5), 2509−2516.
(76) Shpak, A. P.; Korduban, A. M.; Medvedskij, M. M.; Kandyba, V. O. XPS studies of active elements surface of gas sensors based on WO_{3-x} nanoparticles. *J. Electron. Spectrosc. Relat. Phenom.* **2007**, *156*, 172−175.
(77) Lu, Y.; Jia, X.; Ma, Z.; Li, Y.; Yue, S.; Liu, X.; Zhang, J. W^{5+}−W^{5+} Pair Induced LSPR of $W_{18}O_{49}$ to Sensitize ZnIn2S4 for Full-Spectrum Solar-Light-Driven Photocatalytic Hydrogen Evolution. *Adv. Funct. Mater.* **2022**, *32* (35), 2203638.

https://doi.org/10.1021/acsomega.4c10501
ACS Omega 2025, 10, 13080−13104